bioRxiv preprint doi: https://doi.org/10.1101/2020.11.10.375493; this version posted November 10, 2020. The copyright holder for this preprint (which was not certified by peer review) is the author/funder. All rights reserved. No reuse allowed without permission.

Title Page

Hypertrophic cardiomyopathy ß-cardiac myosin mutation (P710R) leads to hypercontractility by disrupting super-relaxed state: multiscale measurements and computational modeling

Alison Schroer Vander Roest*[1], Chao Liu*[2], Makenna M Morck[2], Kristina Bezold Kooiker[1,3], Gwanghyun Jung[1], Dan Song[2] , Aminah Dawood[2], Arnav Jhingran[1], Gaspard Pardon[4], Sara Ranjbarvaziri[1], Giovanni Fajardo[1], Mingming Zhao[1], Kenneth S Campbell[5], Beth L Pruitt[6], James Spudich[2], Kathleen M Ruppel[2], Daniel Bernstein[1]**

***Author Affiliation*:**

[1] Pediatrics (Cardiology), Stanford University, 2200 Biomedical Innovations Building, 240 Pasteur Dr., Palo Alto CA, 94304.

[2] Biochemistry, Stanford University, 405 Beckman Center, 279 Campus Dr. West, Stanford CA 94305

[3] School of Medicine, University of Washington, UW Medicine at South Lake Union, 850 Republican Street, Box 358056, Seattle, WA 98109

[4] Departments of Mechanical Engineering and Bioengineering, Stanford University, School of Engineering and School of Medicine, Stanford, CA, USA

[5] Department of Physiology and Division of Cardiovascular Medicine, University of Kentucky,MS508, 800 Rose Street, Lexington, KY 40536

[6] Bioengineering, University of California, Santa Barbara, Room 3108, University of California, Santa Barbara Santa Barbara, CA 93106-5070

* These authors contributed equally to this work

** *Corresponding Author*:

Daniel Bernstein, M.D.
750 Welch Road Suite 325
Palo Alto, CA 94304
650-723-7913
danb@stanford.edu

bioRxiv preprint doi: https://doi.org/10.1101/2020.11.10.375493; this version posted November 10, 2020. The copyright holder for this preprint (which was not certified by peer review) is the author/funder. All rights reserved. No reuse allowed without permission.

Abstract

Hypertrophic cardiomyopathy (HCM) is the most common inherited form of heart disease, associated with over 1000 mutations, many in β-cardiac myosin (MYH7). Molecular studies of myosin with different HCM mutations have revealed a diversity of effects on ATPase and load-sensitive rate of detachment from actin. It has been difficult to predict how such diverse molecular effects combine to influence forces at the cellular level and further influence cellular phenotypes. This study focused on the P710R mutation that dramatically decreases in vitro motility and actin-activated ATPase, in contrast to other MYH7 mutations. Optical trap measurements of single myosin molecules revealed that this mutation reduced the step size of the myosin motor and the load-sensitivity of the actin detachment rate. Conversely, this mutation destabilized the super-relaxed state in larger, two-headed myosin constructs, freeing more heads to generate force. Micropatterned hiPSC-cardiomyocytes CRISPR-edited with the P710R mutation produced significantly increased force (measured by traction force microscopy) compared with isogenic control cells. The P710R mutation also caused cardiomyocyte hypertrophy and cytoskeletal remodeling, as measured by immunostaining and electron microscopy. Cellular hypertrophy was prevented in the P710R cells by inhibition of ERK or Akt. Finally, we used a computational model that integrates measured molecular changes to demonstrate that closely predict the measured traction forces. These results confirm a key role for regulation of the super-relaxed state in driving hypercontractility in HCM and demonstrate the value of a multiscale approach in revealing key mechanisms of disease.

Keywords: Hypertrophic cardiomyopathy, β-cardiac myosin, hiPSC-CMs, optical trapping, super-relaxed state, traction force microscopy

Significance Statement

Heart disease is the leading cause of death world wide, and hypertrophic cardiomyopathy (HCM) is the most common inherited form of heart disease, affecting over 1 in 200 people. Mutations in myosin, the motor protein responsible for contraction of the heart, are a common cause of HCM but have diverse effects on the biomechanics of the myosin protein that can make it difficult to predict the combined effects of each mutation. We demonstrate that complex biomechanical effects of mutations associated with heart disease can be effectively studied and understood using a multi-scale experimental and computational modeling approach. This work can be extended to aid in the development of new targeted therapies for patients with different mutations.

bioRxiv preprint doi: https://doi.org/10.1101/2020.11.10.375493; this version posted November 10, 2020. The copyright holder for this preprint (which was not certified by peer review) is the author/funder. All rights reserved. No reuse allowed without permission.

Introduction

Hypertrophic cardiomyopathy (HCM) is one of the most prevalent genetic diseases of the heart, affecting over 1 in 200 individuals [1, 2], and is a leading cause of sudden cardiac death [3]. HCM is characterized by cardiomyocyte hypertrophy, myofibril disarray, hypercontractility, and diastolic dysfunction. Tissue remodeling, including interstitial fibrosis, can eventually progress to heart failure and death [4]. Over 1000 causative mutations have been identified, with the majority in genes encoding sarcomeric proteins responsible for generating and regulating contraction. Roughly a third of mutations are located in β-cardiac myosin, the primary ventricular motor protein in humans [5].

With the centrality of hypercontractility in disease phenotypes, HCM mutations were hypothesized to increase the activity of myosin at the protein level, resulting in increased force production at the sarcomere and cellular levels that propagates to the whole organ level [6]. Myosin protein activity is characterized by biochemical and biophysical measurements. The activity of actively-cycling myosin interacting with actin is characterized by the rate of ATP turnover, the rate of detachment from actin, force production, step size, and actin-sliding velocity [7-11]. Myosin that is not actively cycling resides in a super-relaxed state (SRX), associated with a folded-back conformation not available for actin interaction [12]. Biochemical and biophysical assessments of myosin mutations in purified human β-cardiac myosin have revealed various changes in both actively-cycling myosin and SRX proportions [8, 13, 14].

Myosin's converter domain, or hinge responsible for the powerstroke, is a hotspot for pathogenic mutations [9]. The P710 residue is located at the proximal edge of the converter domain, and at least three HCM mutations have been identified at this site, including P710R [15, 16]. A previous report on the P710R mutation found that actively cycling heads have lower ATP turnover activity and duty ratio compared to both WT myosin and other HCM mutations [16]. The discrepancy between this reduced function in actively cycling myosin and the hypercontractile clinical phenotype invites a comprehensive, multiscale assessment of the effects of the P710R mutation on myosin activity and SRX proportions.

In the past, it has been difficult to determine early mechanisms of HCM disease triggered by mutations in β-MHC because of the inability to culture human cardiomyocytes. Samples from hearts obtained at the time of transplant reflect a combination of primary and secondary pathologies. Rodents fail to recapitulate many human heart diseases, and their adult ventricles predominantly expresses the α-MHC isoform, which has different kinetics from β-MHC [17-19]. However, the expansion of CRISPR/Cas-9 protocols for human induced pluripotent derived stem cell (hiPSC) gene editing coupled with efficient differentiation into cardiomyocytes (hiPSC-CMs) provide a valuable model system for studying early mechanisms of disease in a controlled context [18]. In the past, hiPSC-CM models have been limited by the relative immaturity of the

bioRxiv preprint doi: https://doi.org/10.1101/2020.11.10.375493; this version posted November 10, 2020. The copyright holder for this preprint (which was not certified by peer review) is the author/funder. All rights reserved. No reuse allowed without permission.

cardiomyocytes and high population heterogeneity [20]. In traditional two-dimensional culture, these cells have disorganized myofibrils, impaired calcium handling, and immature cell-signaling [21, 22]. However, recent advances in microengineered environments can provide external environmental cues that better recapitulate *in vivo* conditions to promote myofibril alignment and accelerate maturation of both contractile machinery and cell signaling [22, 23]. We have previously developed a hydrogel platform with rectangles of extracellular matrix (ECM) at a 7:1 aspect ratio (similar to that of cardiomyocytes in the left ventricle) that, combined with traction force microscopy (TFM), allows for single-cell assessment of both cellular organization and biomechanics [22-24]. When combined with measurements of myosin function at the molecular level, these cellular measurements can provide key validation of the molecular basis of force generation and resultant disease mechanisms of HCM.

Finally, computational models can provide key insights into the interactions between related dynamic parameters and the resultant implications for the total production of force. Computational models incorpating different degrees of detail and different components of sarcomere structure have been used for decades to answer questions relating to fundamental muscle mechanics [25-32] and alterations to thin filament regulation in the context of cardiac disease and HCM [33, 34]. A new model of myosin activity which incorporates an OFF state representative of the SRX state has recently been validated against experimental measurements of cardiac muscle [35]. This study concluded that force-sensitive regulation of the OFF state significantly improves the fit to experimental data, but this model has not previously been used in the context of MHY7 mutations nor hiPSC-CMs [35].

In this work, we used multi-scale experimental techniques to assess the biomechanical effects of an HCM mutation (P710R) that demonstrates decreased activity at the level of the S1 motor domain yet increased force generation at the cell level. We furthermore used a computational model to integrate the molecular findings and found that altered regulation of the SRX state is an essential driver of hypercontractility for this mutation. Our multi-scale experimental findings combined with computational modeling enabled us to assess the relative contributions of individual molecular parameters to cellular contraction.

Results

Our approach relies on precise biochemical and biomechanical tools for assessing the impact of the P710R mutation in β-cardiac myosin across scales and integrating our results using a validated computational model.

bioRxiv preprint doi: https://doi.org/10.1101/2020.11.10.375493; this version posted November 10, 2020. The copyright holder for this preprint (which was not certified by peer review) is the author/funder. All rights reserved. No reuse allowed without permission.

The P710R mutation reduces load sensitivity and step size of single myosin molecules

We first focused on the motor domain of myosin, using a recombinant human β-cardiac myosin sS1 domain (catalytic domain plus the essential light chain binding portion of the lever arm). The properties of individual myosin heads interacting with actin were assessed by optical trapping using harmonic force spectroscopy (HFS). In this technique, the durations of binding events between a single myosin and an actin filament under different load forces are measured in physiological (2 mM) ATP conditions. The sample stage oscillates sinusoidally so that by the randomness of where myosin initially attaches to actin, a range of mean forces are automatically applied over the course of many binding events [11]. This technique has been used to quantify changes in the load-dependent detachment rate of β-cardiac myosin due to mutations and myosin inhibitor and activators [10].

The detachment rate is an exponential function of load force (F):

$$k_{det}(F, \Delta F) = k_0 I_0\left(\frac{\Delta F \delta}{k_B T}\right) e^{\frac{-F\delta}{k_B T}} \qquad \text{Eqn. 1}$$

where k_0 is the rate at zero load, δ is the distance to the transition state of the rate-limiting step in the bound state (a measure of force sensitivity), k_B is the Boltzmann constant, T is temperature, and I_0 is the zeroth-order modified Bessel function of the first kind (to correct for the harmonic force with amplitude ΔF). WT β-cardiac myosin has detachment rate at zero load k_0 = 104 ± 5 s^{-1} and force sensitivity δ = 1.39 ± 0.06 nm, consistent with previous results [10, 11, 36, 37]. The unloaded detachment rate of P710R is not significantly changed (87 ± 5 s^{-1}, p = 0.12), while δ is dramatically reduced (0.31 ± 0.03 nm, p < 0.0001) (**Table 1** and **Figure 1AB**).

Table 1: Parameters measured for β-cardiac myosin sS1. k_0, δ and step size were measured from single molecules using the HFS technique. k_{cat} and K_{app} were measured using a colormetric actin-activated ATPase assay and were previously reported [16]. Unloaded velocities were measured by the motility assay with actin filaments. Calcium sensitivity parameters pCa_{50} and Hill coefficient n were measured by motility assay with regulated thin filaments. Data are presented as mean ± standard error of the mean. * signifies p < 0.05 and **** signifies p < 0.0001 different between P710R and WT

	k_0 (s^{-1})	δ (nm)	Step size (nm)	k_{cat} (s^{-1})	K_{app} (μM)	Velocity (nm/s)	pCa_{50}	n
WT	104 ± 10	1.39 ± 0.06	5.2 ± 0.3	4.1 ± 0.4	33 ± 6	762 ± 16	6.46 ± 0.04	2.2 ± 0.2
P710R	87 ± 5	0.31 ± 0.03****	1.9 ± 0.3****	2.50 ± 0.1*	14 ± 1*	239 ± 9****	6.48 ± 0.07	3.1 ± 0.6

bioRxiv preprint doi: https://doi.org/10.1101/2020.11.10.375493; this version posted November 10, 2020. The copyright holder for this preprint (which was not certified by peer review) is the author/funder. All rights reserved. No reuse allowed without permission.

Further analysis of the average trapped bead displacement during binding events revealed that the mutation decreases myosin's step size by ~60% (WT d = 5.2 ± 0.3 nm, P710R d = 1.9 ± 0.3 nm, p < 0.0001) (**Table 1, Figure 1CD, Figure S1**).

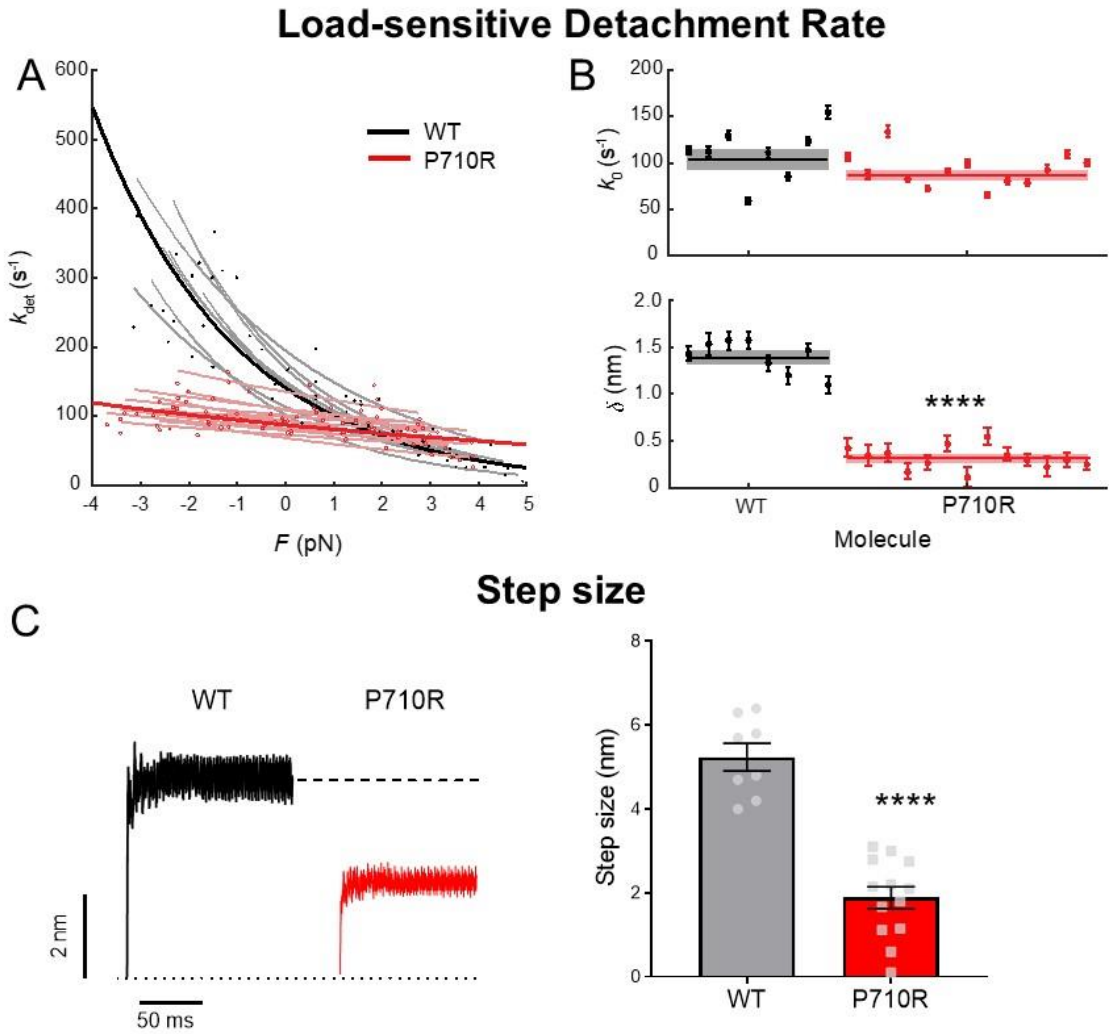

Figure 1: Single molecules of β-cardiac myosin sS1 with P710R mutation have reduced load sensitivity and step size. (A) Measurements of myosin's load sensitive rate of detachment from actin $k_{det}(F)$ using the harmonic force spectroscopy technique in a dual-beam optical trap. Positive forces represent load in the opposite direction of the powerstroke (resistive), and negative forces respresent load in the same direction of the powerstroke (assistive). Each light line in is a fit of Eqn. 1 to data from one molecule, each with a few hundred binding events. Error bars on data points are not shown for clarity. **(B)** The fitted parameters k_0 (rate at zero load) and δ (load sensitivity parameter) of each molecule corresponding to light lines in (A). Horizontal lines represent weighted means, and shaded rectangle represent s.e.m. (**C**) Averaged start-aligned position traces of binding events from two example molecules revealing the power stroke of myosin, which occur within milliseconds of actin binding. Step size values of multiple molecules are shown on the right. Values are given in Table 1. See also methods and Figure S1. **** indicates p < 0.0001.

bioRxiv preprint doi: https://doi.org/10.1101/2020.11.10.375493; this version posted November 10, 2020. The copyright holder for this preprint (which was not certified by peer review) is the author/funder. All rights reserved. No reuse allowed without permission.

The P710R mutation reduces k_{cat}, duty ratio, and velocity, but not calcium sensitivity of myosin in ensemble

We next assessed the effects of the P710R mutation on properties of myosin sS1 in ensemble. P710R has significantly reduced actin-activated ATPase activity (WT k_{cat} = 4.1 ± 0.4, P710R k_{cat} = 2.50 ± 0.1) and higher apparent actin affinity (WT K_{app} = 33 ± 6, P710R K_{app} = 14 ± 1) as reported previously [16] (**Table 1)**. Given the single molecule and ensemble ATPase meaurements, the duty ratio can be estimated as a function of load force (*F*) [10]:

$$dr(F) = \frac{k_{attach}}{k_{attach}+k_{det}(F)} \qquad \text{Eqn. 2}$$

where the attachment rate k_{attach} is given by

$$k_{attach} = \frac{1}{1/k_{cat}-1/k_0}. \qquad \text{Eqn. 3}$$

Our calculations suggest that P710R has a much lower duty ratio than WT myosin at low or resistive (positive) loads (**Figure 2A**), consistent with a previously reported prediction [16]. Since duty ratio is the fraction of heads bound to actin in a force-producing state at any given time, P710R is predicted to generate less force per head on average than WT at those loads. Our calculations predict that P710R has a slightly higher duty ratio than WT under high assistive (negative) loads, suggesting that P710R heads may not relase actin as efficiently in an actively shortening sarcomere.

Actin sliding velocity in an unloaded motility assay was reduced by ~60% for P710R compared to WT (**Figure 2B**, Figure S2). Velocity can be approximated as the step size divided by the actin-bound time, which is inversely proportional to the actin detachment rate: $v = d/t_{bound} = d*k_{det}$. Thus, the 60% reduction in motility velocity can be explained by the ~60% reduction in P710R's step size and an unchanged detachment rate k_0. A previous study of this mutation failed to predict the measured decrease in motility likely because the authors did not account for a major reduction in step size [16]. We further observed that 5-15% of actin filaments were immobile for P710R compared to 0-5% for WT (Figure S2). This suggests that the mutation may induce a less proper or stable protein fold in a small percentage of myosin molecules which, as a result, have reduced function in moving actin (see also methods and discussion).

In addition to determining motility velocity, myosin's actin-detachment kinetics may affect the calcium sensitivity of sarcomeres through the activation of the thin filament by cooperatively-binding myosin heads [38]. In the thin filament, binding sites on actin are blocked by the regulatory proteins troponin and tropomyosin when calcium levels are low (in diastole) and are activated and accessible to myosin heads when calcium levels rise (in systole). However, heads that stay bound to actin longer may cooperatively activate the thin filament at lower calcium concentrations [39, 40], thereby altering the calcium sensitivity. While P710R has an unchanged unloaded actin-detachment rate k_0, the effect

bioRxiv preprint doi: https://doi.org/10.1101/2020.11.10.375493; this version posted November 10, 2020. The copyright holder for this preprint (which was not certified by peer review) is the author/funder. All rights reserved. No reuse allowed without permission.

of its reduced force sensitivity δ on this mechanism of calcium sensitivity is unclear. To this end, we measured the sliding velocities of regulated thin filaments (RTF, actin decorated with troponin and tropomyosin) at various calcium concentrations in the motility assay. RTF velocities increase as calcium concentration is increased through the physiological range (pCa7-6, or 100 nM to 1 μM), and velocities saturate at high calcium levels (pCa4) (**Figure 2C**). We found that the P710R mutation does not significantly affect the calcium sensitivity; neither the calcium concentration for half-maximum velocity (P710R pCa50 = 6.48 ± 0.07, WT pCa50 = 6.46 ± 0.04, p = 0.78) nor the Hill coefficient (P710R n = 3.1 ± 0.6, WT n = 2.2 ± 0.2 , p = 0.23) are significantly different from WT (**Table 1**; **Figure 2C**).

Taken together, the above measurements of the myosin motor domain at the single molecule and ensemble levels do not suggest a clear mechanism of hypercontractility by the HCM mutation P710R. In fact, they appear to suggest hypocontractility, in conflict with the mutation's physiological effects in patients.

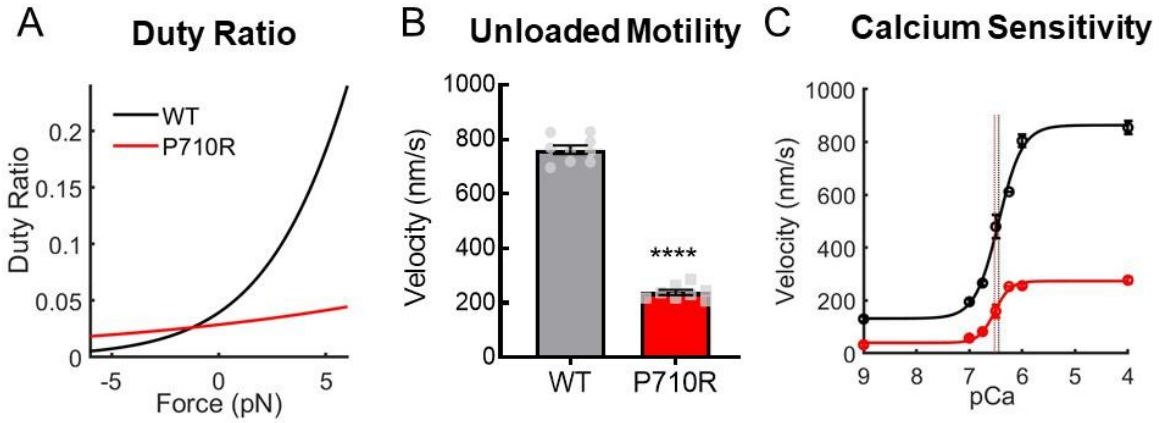

Figure 2: β-cardiac myosin sS1 ensembles with P710R mutation have altered duty ratio, reduced actin sliding velocity, and unchange calcium sensitivity. (**A**) Calculated duty ratio across load forces based on ATPase and actin detachment rate measurements. (**B**) Actin sliding velocity (mean velocity including stuck filaments, MVIS; see methods) in the unloaded motility assay. (**C**) Velocities (MVIS) of regulated thin filaments at various calcium concentrations measured by the motility assay. pCa = -log[Ca]. Curves are fits to the Hill equation of averaged data from multiple independent experiments, and vertical dashed lines represent the fitted pCa50's. Error bars represent s.e.m. Values are given in Table 1. See also Figure S2. **** indicates p < 0.0001.

bioRxiv preprint doi: https://doi.org/10.1101/2020.11.10.375493; this version posted November 10, 2020. The copyright holder for this preprint (which was not certified by peer review) is the author/funder. All rights reserved. No reuse allowed without permission.

The P710R mutation disrupts the SRX state of myosin in vitro

We have previously shown that the ability of myosin to form the folded-back interacting-heads motif structure is critical for regulating myosin activity, and many HCM-causing mutations appear to disrupt the ability of myosin to enter this state [8, 13, 14]. To assess the ability of myosin to form this folded-back "off" state *in vitro*, we used 2-headed myosin constructs as previously described [14]. We have previously observed a ~40% reduction in the actin-activated ATPase rate (k_{cat}) of a long-tailed (25-hep) WT myosin construct compared to a short-tailed (2-hep) WT construct (2-hep k_{cat} = 7.2 ± 0.7 s^{-1}, 25-hep k_{cat} = 4.1 ± 0.3 s^{-1}, p = 0.004) (**Figure 3A,B**). This difference can be attributed to the sequestration of a large fraction of the myosin in the folded-back state in the long-tailed population, thus preventing the heads from binding to actin and entering the ATPase cycle. In contrast, we found no significant difference between the ATPase rate of the P710R short- and long-tailed myosins (P710R 2 hep k_{cat} = 4.5 ± 0.3 s^{-1}, P710R 25 hep k_{cat} = 4.3 ± 0.3 s^{-1}, p = 0.52) (**Figure 3C**). This suggests that P710R has a greatly reduced ability to access the sequestered folded-back state.

We have previously correlated the folded-back structural state with the proportion of basal ATP turnover at the SRX rate (~0.003 s^{-1}), as opposed to the disordered relaxed state (DRX) rate (~0.01 – 0.03 s^{-1}) [13].These rates are measured using a single mant-ATP turnover assay in the absence of actin, in which the release of fluorescent mant-ADP from myosin is measured over time. The signal shows a biexponential decay characterized by two rates: the faster rate corresponds to the DRX rate, and the slower rate corresponds to the SRX rate (**Figure 3D**). Lower fractions of SRX correlate with a reduced ability to form the folded-back state (via EM imaging and ATPase [13]). We have previously showed that the percentage of WT 25-hep myosin hydrolyzing ATP at the slower SRX rate was 55-65% (at a salt concentration of 5 mM KOAc), in contrast to WT 2-hep myosin, which shows 15-25% SRX (regardless of salt concentration) due to its inability to form the folded-back state (**Figure 3F**) [8]. Here, we found no significant difference in percentage SRX between WT and P710R 2-hep myosins (p = 0.12, Figure 3F). In contrast to WT 25-hep, only 27 ± 6% of the P710R 25-hep myosin hydrolyze ATP at the slow rate (p = 0.0001 vs. WT 25-hep, **Figure 3F**). The fast rate of P710R 2-hep myosin was higher than that of WT 2-hep myosin (p = 0.004, Table S1), while the fast rate of P710R 25-hep myosin was not significantly different from that of WT 25-hep myosin. Consistent with our 25-hep ATPase findings, these single-turnover results confirm that the P710R mutation reduced myosin's ability to form the folded-back SRX state.

To summarize our molecular studies, the P710R mutation significantly reduced the load sensitivity of the detachment rate from actin, step size, and unloaded motility, suggesting hypocontractility. However, the mutation also reduced the ability of myosin to form the SRX state, suggesting hypercontractility. Thus, to understand these competing effects, we next investigated the effects of this mutation in human cardiomyocytes.

bioRxiv preprint doi: https://doi.org/10.1101/2020.11.10.375493; this version posted November 10, 2020. The copyright holder for this preprint (which was not certified by peer review) is the author/funder. All rights reserved. No reuse allowed without permission.

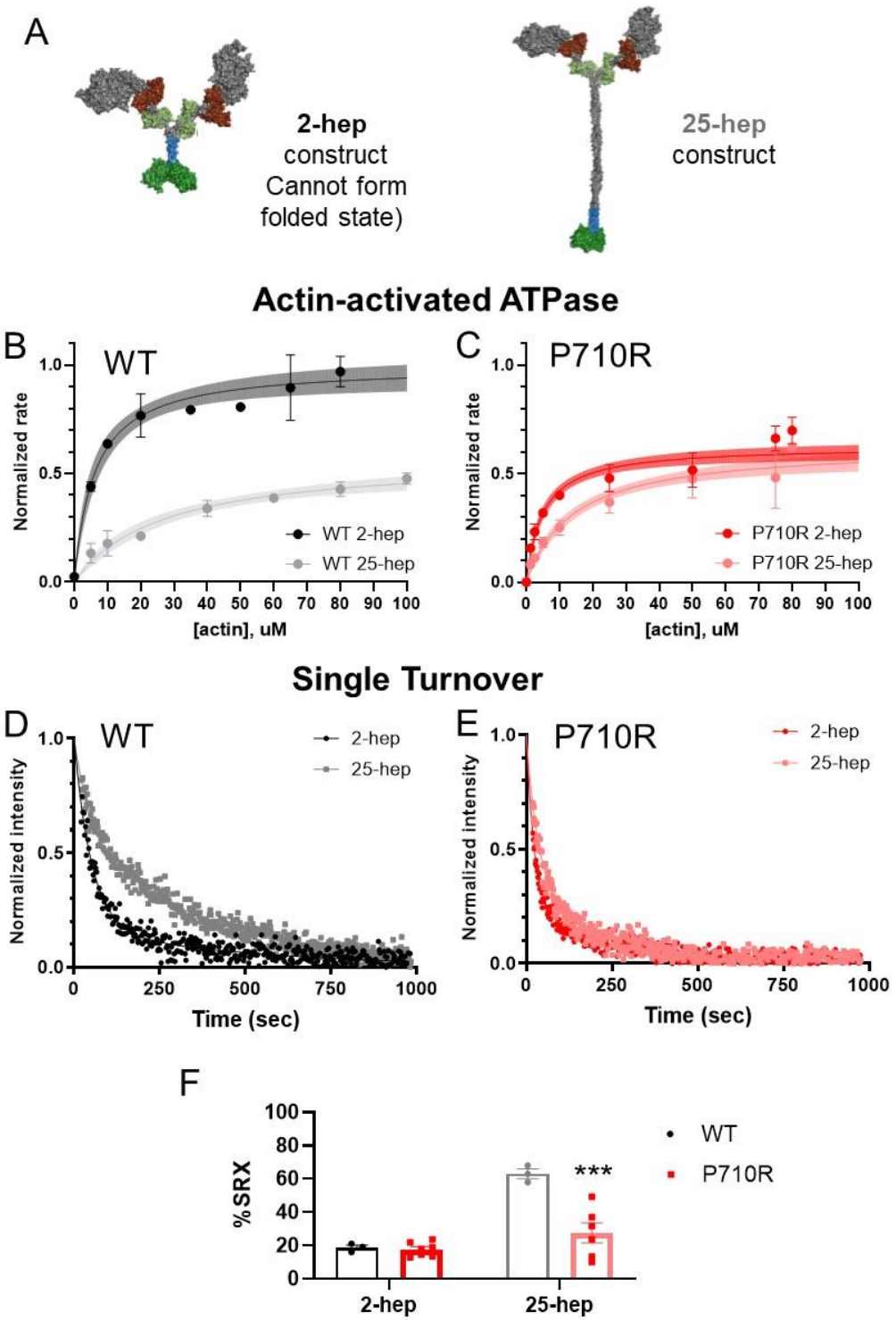

Figure 3: β-cardiac myosin ensembles with P710R mutation have reduced SRX state. (A) Schematic of protein constructs show 2 head (S1) domains (with light chains) and a 2 or 25-heptad tail domain. (**B-C**) Ensemble measurement of actin-activated ATPase rate normalized to the k_{cat} for the WT 2-hep. (**D-E**) Mant-ATP single turnover in the short (2-hep) and long (25-hep) tailed protein constructs. (**F**) Quantification of the %SRX in both WT and P710R myosins. WT data (D-F) was previously reported [8].

bioRxiv preprint doi: https://doi.org/10.1101/2020.11.10.375493; this version posted November 10, 2020. The copyright holder for this preprint (which was not certified by peer review) is the author/funder. All rights reserved. No reuse allowed without permission.

The P710R mutation increases traction force generation and cell size in micro-patterned hiPSC-CMs

We used CRISPR/Cas9 gene editing to insert a point mutation of proline to arginine in one allele of the MYH7 gene (Figure S4). We first measured the effects of the P710R mutation on cellular force generation using traction force microscopy (TFM). Isolated hiPSC-CMs at 35-40 days after cardiac differerentiaton were cultured for 4-5 days on hydrogels of physiologic stiffness (10kPa) with matrigel bioprinted in a mature cardiomyocyte aspect ration of 7:1 [22, 24]. We have previously shown that this platform optimizes force generation and dramatically enhaces hiPSC-CM maturation [22]. hiPSC-CMs with the P710R mutation produced significantly higher total peak force than WT controls (**Figure 4 A-B**). Our single cell platform allowed assessment of >30 cells per group from three differentiation batches (**Figure 4C**) and provides spatially and temporally resolved measurements of traction force for each cell. We also observed a significant increase in the contraction duration in the P710R cells (**Figure 4D**). P710R cells were significantly larger than the WT (**Figure 4E**), and the significant increase in force persisted after normalizing peak force to cell area (**Figure 4F**).

bioRxiv preprint doi: https://doi.org/10.1101/2020.11.10.375493; this version posted November 10, 2020. The copyright holder for this preprint (which was not certified by peer review) is the author/funder. All rights reserved. No reuse allowed without permission.

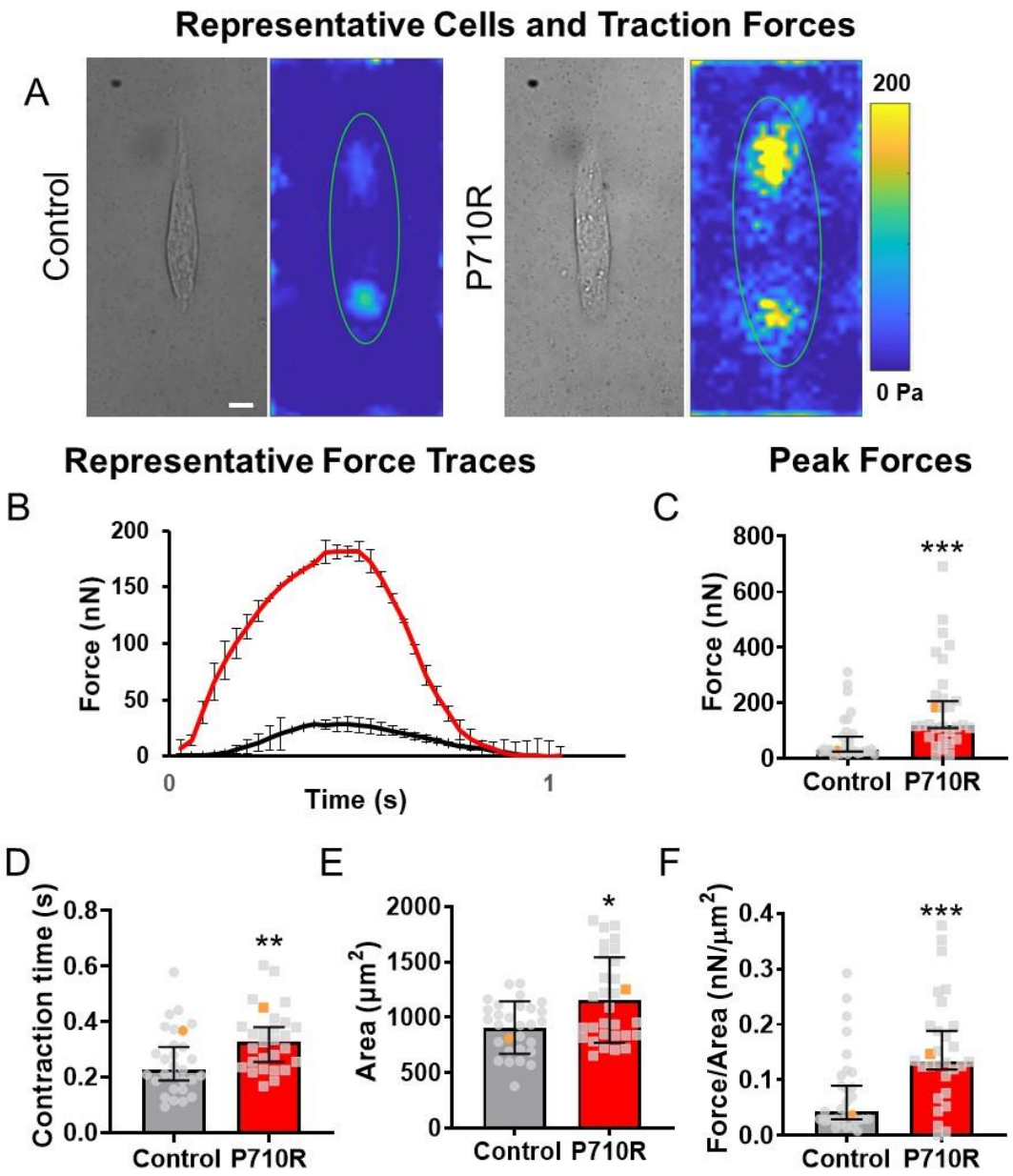

Figure 4: P710R mutation in micropatterned single hiPSC-cardiomyocytes significantly increases contractile function. (**A**) Representative single cells shown in bright field and as peak traction force plots (scale bar represents 10 μm). (**B**) Multiple (2-4) beats were captured per cell and the averaged traces for representative cells are shown, with error bars representing the standard deviation of force between beats. (**C**) Peak forces of single control (n = 30) and P710R (n = 31) cells collected from 3 differentiation batches. (**D**) The contraction time of each cell was measured as the time between peak velocity of contraction and peak velocity of relaxation. (**E**) The median cell area was measured and used to calculate (**F**) cell force normalized to cell area. Representative cells are identified with orange markers in plots of population (n-30-31 cells). Data are presented as median ± 95% confidence interval. * indicates $p < 0.05$, ** indicates $p < 0.01$, *** indicates $p < 0.001$.

bioRxiv preprint doi: https://doi.org/10.1101/2020.11.10.375493; this version posted November 10, 2020. The copyright holder for this preprint (which was not certified by peer review) is the author/funder. All rights reserved. No reuse allowed without permission.

The P710R mutation causes myofibril disruption and z-disk thickening in patterned hiPSC-CMs

The ability of myosin to generate contractile forces *in vivo* depends on its incorporation into sarcomeres and myofibrils. Staining for β-MHC revealed organization into sarcomeres in cells grown on patterned hydrogels (**Figure 5A**). While there was a substantial amount of variability in quality of myofibril organization within the population, we observed markedly disorganized sarcomere structures in many of the immunostained images in P710R mutant cells compared with WT, consistent with the human disease phenotype. Sarcomere lengths were not significantly different between control and mutant cells when quantified from immunostained cells (**Figure 5B**). We confirmed this result using transmission electron microscopy (TEM) (**Figure 5C-D**). TEM of patterned cells showed aligned myofibrils in the WT controls and varying degrees of myofibril and sarcomeric disruption in many P710R cells. The degree of myofiber disarray was quantified using the directionality tool in ImageJ, and the degree of dispersion of directionality across the image was significantly increased in P710R cells (**Figure 5E**). We also observed significant thickening (measured along fiber direction) of the z-disks in P710R cells (**Figure 5F**). This cytoskeletal disruption may be an indication of cellular remodeling which ultimately leads to hypertrophy.

bioRxiv preprint doi: https://doi.org/10.1101/2020.11.10.375493; this version posted November 10, 2020. The copyright holder for this preprint (which was not certified by peer review) is the author/funder. All rights reserved. No reuse allowed without permission.

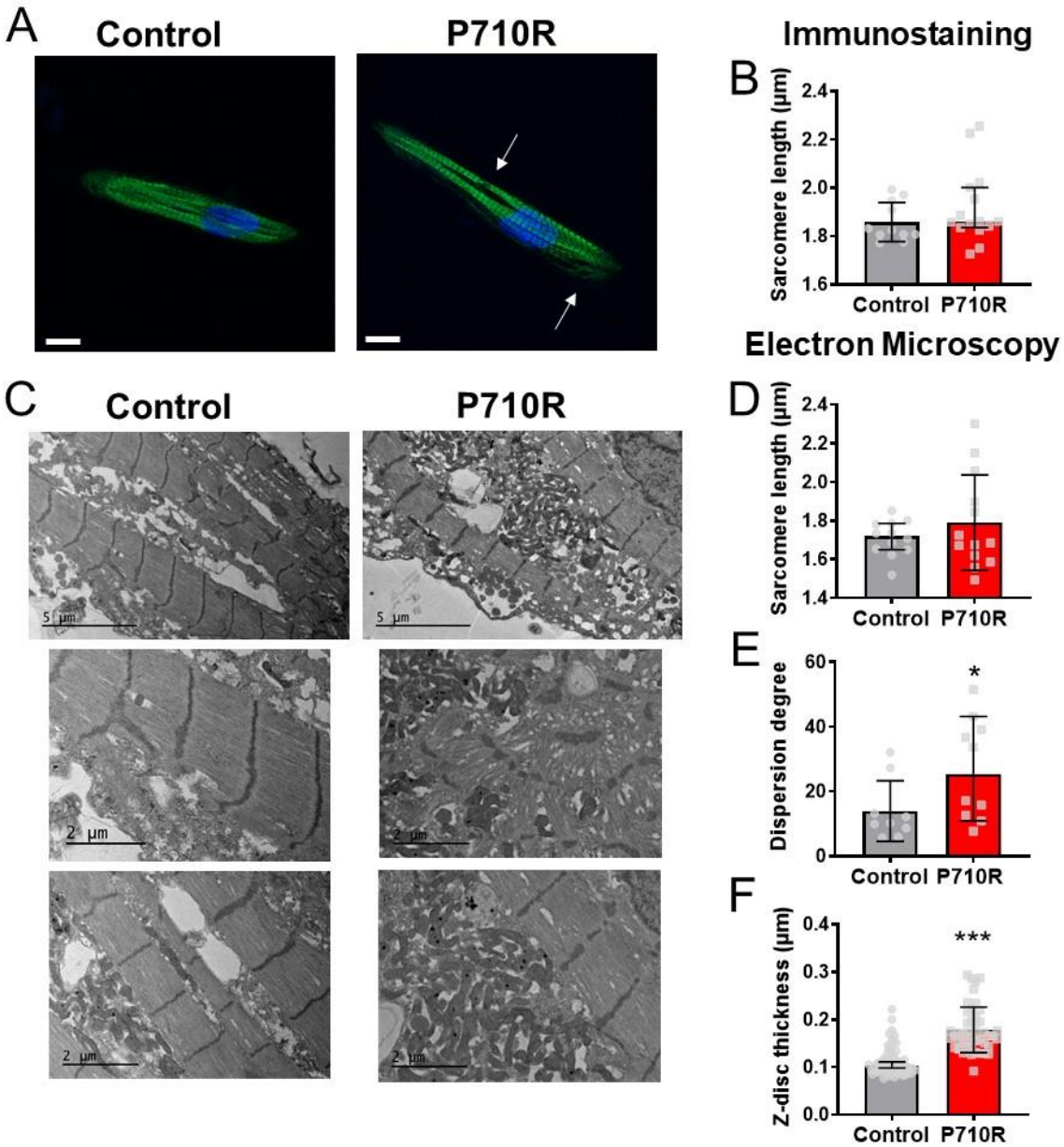

Figure 5: P710R mutation in micropatterned hiPSC-cardiomyocytes significantly disrupts myofibril organization. (**A**) Immunostaining of β-cardiac myosin in micropatterned cells (scale bar equals 10 µm, sarcomere disruption is marked with arrows) enabled (**B**) quantification of sarcomere length in micropatterned cells. (**C**) Representative transmission electron microscopy images of patterned cells enabled (**D**) quantification of sarcomere length, (**E**) dispersion degree, a measure of myofibril alignment, and (**F**) z-disk thickness from TEM images. Data are presented as median ± 95% confidence interval. * indicates $p < 0.05$.

bioRxiv preprint doi: https://doi.org/10.1101/2020.11.10.375493; this version posted November 10, 2020. The copyright holder for this preprint (which was not certified by peer review) is the author/funder. All rights reserved. No reuse allowed without permission.

The P710R mutation causes hypertrophic growth of hiPSC-CMs via Akt and ERK

We next tested whether the P710R mutation increases cell size across the broader population of cells (and not only in paceable, patterned cells). After 45 days of culture in confluent monolayers, hiPSC-CMs were replated sparsely onto Matrigel coated tissue culture plastic, allowed to attach and spread for 2 days, and then fixed and stained to quantify their spread area. P710R cells were significantly larger than the control cells (**Figure 6A**). Western blot analysis of two known hypertrophic growth signaling pathways showed increased ERK and Akt basal activation (**Figure 6B-C**) in P710R cells. Inhibition of these signaling proteins with previously characterized specific inhibitors (SCH772984 and Akt i 1/2) [41, 42] between day 26 and 46 resulted in significantly reduced cell area in P710R cells relative to untreated P710R cells (**Figure 6D**). However, the treatment of P710R cells with either inhibitor did not fully reduce their area to the size of the corresponding inhibitor treated unedited control cells (Figure S5).

We also quantified the relative expression of β-MHC and α-MHC in P710R cells compared to isogenic control cells with both western blot and qPCR (Figure S6). We found no significant difference in β-MHC protein or transcript levels between P710R and control cells, while α-MHC protein and transcript levels were significantly reduced in P710R cells compared to control. However, the relative transcript levels of MYH6 to MYH7 was less than 0.1, suggesting that the majority of myosin heavy chain in both isogenic control and P710R cells was MYH7.

bioRxiv preprint doi: https://doi.org/10.1101/2020.11.10.375493; this version posted November 10, 2020. The copyright holder for this preprint (which was not certified by peer review) is the author/funder. All rights reserved. No reuse allowed without permission.

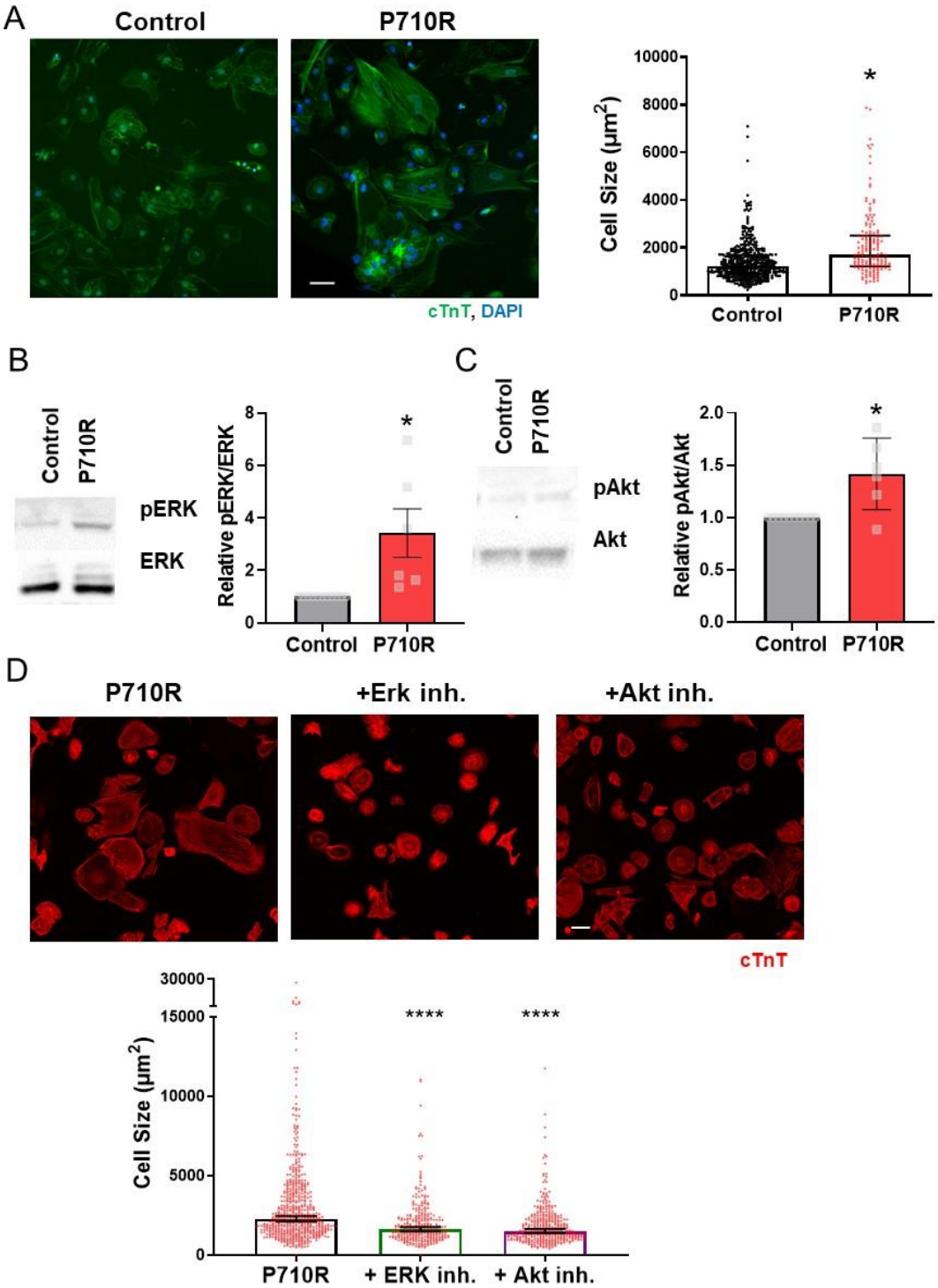

Figure 6: P710R mutation in hiPSC-cardiomyocytes significantly increases cell size and activation of proteins involved in hypertrophic signaling. (**A**) Size of unpatterned cells was quantified from immunostaining for cardiac troponin T (cTnT). (**B**) and (**C**) Western blot analysis of phosphorylation of the hypertrophic signaling pathway proteins ERK (B) and (C) Akt in unpatterned cells with each P710R sample normalized to matched isogenic control. (**D**) Quantification of cell size after treatment of P710R cells with specific inhibitors of ERK and Akt. Scale bar represents 50 microns. Graphs of cell area are presented as median ± 95% confidence interval. * indicates $p < 0.05$ and *** indicates $p < 0.001$.

bioRxiv preprint doi: https://doi.org/10.1101/2020.11.10.375493; this version posted November 10, 2020. The copyright holder for this preprint (which was not certified by peer review) is the author/funder. All rights reserved. No reuse allowed without permission.

Computational modeling of P710R myosin compared to WT predicts an increase in force when SRX disruption was included

To determine the predicted effects of individual and combined changes in myosin kinetics on total force production, we used a previously validated computational model of cardiac muscle contraction [35], modified to contain an exponential load dependent detachment rate (**Figure 7A** and Figure S7). This model includes an OFF state to represent the SRX state of myosin. We measured calcium transients in monolayers of isogenic control and P710R cells when paced at 1 Hz (Figure S8), scaled the transients to the range of calcium concentration previously published for this model, and used the scaled transients as inputs to this model [43] (**Figure 7B**). We incorporated in this model the measured unloaded detachment rate (k_0), its load sensitivity (δ), and step size. We defined the rate of myosin attachment (k_A) from the previous modeling analysis that used our steady state actin-activated ATPase measurements for sS1 [16] (see methods for more details).

We did not directly measure the rates of transitioning into and out of the SRX state, but we did measure significant differences in the percentage of myosins in the SRX state between WT and P710R in the presence or absence of actin. After identifying a set of parameters that successfully predicted the measured force output of a representative control cell (normalized to cross-sectional area), we found a best fit for the relative increase in rate of opening from the OFF state (k_{-SRX}) to fit the force output of a representative P710R cell (see methods and Figure S9). This process determined that a 12.9 fold increase in $k_{-\mathrm{SRX}}$ provided the optimal fit (mean normalized deviation 1.23 [35]) to the representative data. An increase in $k_{-\mathrm{SRX}}$ is consistent with the decrease in functional SRX state we measured experimentally, and the model predicted SRX% to be lower for the P710R cell at both contracted and relaxed periods of the cardiac cycle (Figure S8D). The rate of entering the SRX state (k_{+SRX}) was set to 200 s^{-1} for both groups based on published data and previous modeling [35, 44]. All other parameters were held constant between control and P710R, including the rates of thin filament activation (k_{on}), inactivation (k_{off}), and the cooperativity coefficient (k_{coop}). The changes to myosin kinetics ($k_{-\mathrm{SRX}}$, k_0, δ and step size) were sufficient to increase the percentage of thin filament activation and binding over the time course of contraction (**Figure 7C**).

The force predicted by the model after fitting parameters (Table S2) agreed well with the representative force traces (**Figure 7D**) and with the median force normalized to cross-sectional area of the population of cells (**Figure 7E**). Sensitivity analysis (Figure S9) suggested that four fold changes in cross bridge density up and down spans the range of 90% of the cell forces we measured and matches the distribution of cell data. This parameter incorporates both the number of myosin heads per myofibril (which may vary with cell maturity and myofibril disruption) and the density of myofibrils in a cell (which we observed to be variable in these cells - Figure S10). Further simulations using the best fit parameter set and independently adding or removing each of the four measured

bioRxiv preprint doi: https://doi.org/10.1101/2020.11.10.375493; this version posted November 10, 2020. The copyright holder for this preprint (which was not certified by peer review) is the author/funder. All rights reserved. No reuse allowed without permission.

parameters revealed that modulation of the rate of exiting the SRX state accounts for the majority of the measured increase in force (**Figure 7F**). An important note is that this analysis does not necessarily prove that the basal rate of opening from the SRX state is specifically increased, as opposed to an equivalent reduction in the rate of returning to the SRX state (Figure S9). Both our sensitivity analysis (Figure S11) and additional fitting suggest (Figure S9A) that the effects of changing $k_{\text{-SRX}}$ and $k_{\text{+SRX}}$ are nearly mirrored. Our results support the hypothesis that a change in the equilibrium between the SRX state and actively cycling states is essential for the P710R mutation to produce significant hypercontractility.

In summary, our cellular experiments confirm a hypercontractile and hypertrophic phenotype in hiPSC-CMs harboring the P710R mutation. Furthermore, our modeling results suggest that the measured molecular effects of P710R are consistent with hypercontractility if and only if SRX regulation is included.

bioRxiv preprint doi: https://doi.org/10.1101/2020.11.10.375493; this version posted November 10, 2020. The copyright holder for this preprint (which was not certified by peer review) is the author/funder. All rights reserved. No reuse allowed without permission.

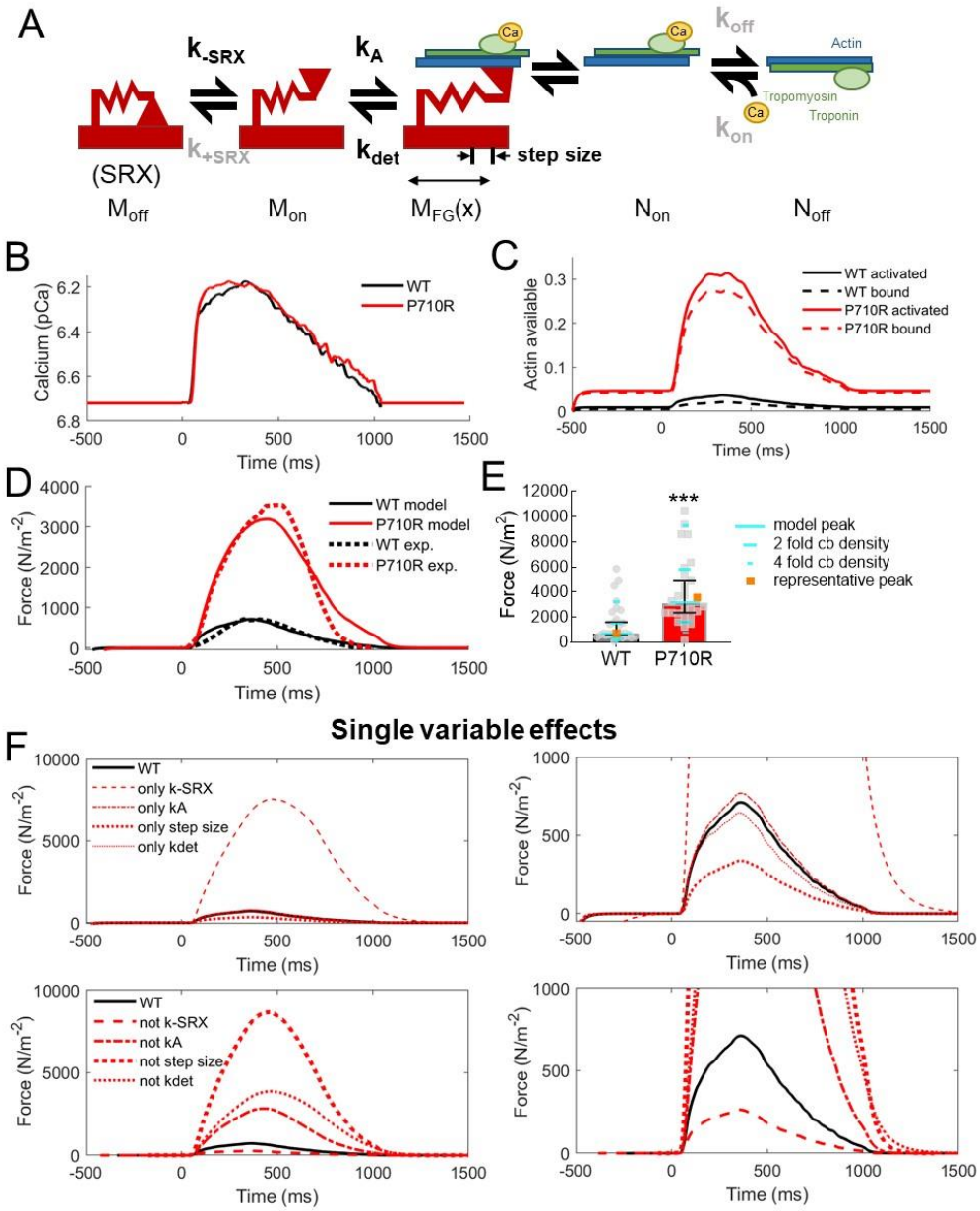

Figure 7: Modeling effects of P710R mutation highlight the importance of modulation of the SRX state to observe hypercontractility. (**A**) Model schematic with adaptation of detachment rate to incorporate an exponential dependence on load. M_{off}, M_{on} and $M_{FG}(x)$ represent the different states of myosin. N_{on} and N_{off} represent available and deactivated thin filaments, respectively. Parameters estimated or fit from *in vitro* experiments are shown in black, while rates held constant between groups are shown in gray. (**B**) Calcium transients measured in cellular monolayers were used as an input for the model. The model predicted (**C**) actin availability (fraction bound to myosin shown with dashed line) and (**D**) contractile force (solid line) , which was fit to force traces from representative cells (dashed lines) normalized to cell cross-sectional area. (**E**) The predicted peak force (teal) fell close to the median measured force in our cell population when normalized to cross-sectional area, and two to four-fold changes to cross-bridge (cb) density relatively match the measured distribution of data. Representative cells highlighted in orange. (**F**) Simulations of independent effects of the four parameters (by inclusion with WT parameters and replacing from the best-fit mutant parameters). Zoomed in plots are included to improve visualization of low force traces.

bioRxiv preprint doi: https://doi.org/10.1101/2020.11.10.375493; this version posted November 10, 2020. The copyright holder for this preprint (which was not certified by peer review) is the author/funder. All rights reserved. No reuse allowed without permission.

Discussion

The diversity and complexity of molecular alterations associated with HCM have made predictions of disease penetrance, severity, and response to therapeutics quite challenging. Our study demonstrates the power of an integrated, multiscale approach to study the biomechanical effects of mutations in myosin known to cause HCM. The P710R mutation was previously reported to have reduced ATPase activity and motility velocity, suggesting in isolation that it should reduce duty ratio and cause hypocontractility at the cellular level [16]. In the present work, integrating molecular measurements of single molecules and ensembles of single and two-head constructs provides a more complete picture of the molecular mechanisms which contribute to the hypercontractility observed *in vivo*. By combining both a cellular model system and computational modeling, we were able to validate the hypercontractile effect of this mutation, demonstrate additional HCM-associated phenotypes, and provide key insights into the driving factors by which myosin mutations can result in hypercontractility in HCM.

Single molecules of β-cardiac myosin with the P710R mutation have reduced step size d, preserved actin detachment rate under zero load k_0, and reduced load sensitivity δ of the actin detachment rate (**Figure 1**). This combination of findings suggest a possible molecular mechanism described as follows. In WT myosin, the converter domain, where P710 resides, couples the swing and forces at the lever arm to the conformational changes and forces at the nucleotide pocket. Through this coupling, load on the lever arm affects the rate of release of ADP from the pocket, which determines the actin detachment rate k_{det}. In P710R myosin, the proline to arginine substitution may disrupt the local structure of the converter domain, resulting in a reduction in the described coupling. Consequently, the rate of ADP release (the actin detachment rate k_{det}) is less dependent on load force (smaller δ) because load placed on the lever arm is no longer fully conveyed to the nucleotide pocket. Similarly, the step size d is reduced because the conformational change at the pocket is no longer fully conveyed to the lever arm. The unloaded ADP release rate (unloaded actin detachment rate k_0) is not affected by the mutation presumably because the local structure of the nucleotide pocket remains intact. Due to inherent variability among individual molecules, as evident in our single molecule data (Figure 1), the extent of disruption by P710R may vary. Thus, P710R may cause a small percentage of molecules to be fully dysfunctional in moving actin ("deadheads"), resulting in the observed higher numbers of immobile actin filaments in the motility assay (Figure S2).

We have previously observed reductions in the load sensitivity of myosin's actin detachment rate by cardiac myosin effectors but not by cardiomyopathy causing mutations [10]. For example, the investigational heart failure drug omecamtiv mecarbil (OM) dramatically reduces the detachment rate, its load sensitivity [10], and myosin's step size [37]. As the effects of OM and P710R share some similarities, it is important to note

bioRxiv preprint doi: https://doi.org/10.1101/2020.11.10.375493; this version posted November 10, 2020. The copyright holder for this preprint (which was not certified by peer review) is the author/funder. All rights reserved. No reuse allowed without permission.

that residue P710 is part of the OM binding pocket in the converter domain [45]. A recent preprint reported a reduction in myosin's step size due to a different HCM mutation in the same region (P712L) [46]. Taken together, these results emphasize the converter domain's critical facilitation of myosin's powerstroke and load sensitivity and reveal various consequences of perturbing this domain.

A major finding of this study is that the disruption of the folded, SRX state is a critical driver of hypercontractility with the P710R mutation. The results of the actin-activated ATPase and single-turnover experiments using the longer tailed 25-hep construct (**Figure 3**) demonstrate that a significantly larger fraction of myosins with this mutation are in an open, more active state than WT control. This increases the number of heads available for binding to actin, which we hypothesized would increase force production. We have measured similar changes in SRX across a range of HCM-causing mutations [8, 14], and others have confirmed these effects in cellular and animal models [13, 47], suggesting that SRX regulation may be a major cause of hypercontractility in HCM. This is further corroborated by the finding that mavacamten, a small-molecule inhibitor of myosin that is known to increase the SRX state, is effective in reducing symptoms in patients with HCM [13, 48]. Our computational modeling analysis also supports the importance of destabilization of the SRX for increasing net force even when combined with a hypocontractile change like decreased step size.

We confirmed that the P710R mutation causes hypercontractility and other key features of HCM in cardiomyocytes using a cellular experimental model in parallel with molecular level experiments. Using a micropatterned culture system also allowed for measurement of cellular scale forces that are enhanced by the alignment of myofibrils and balanced by a physiologic-range substrate stiffness (10 kPa). This system has also been used to quantify hypercontractility in hiPSC-CMs with HCM-causing troponin mutations [49]. The transverse force we measured in the cells was significantly lower than what has been reported for mature cardiac tissue, but this is a known sign of the relative immaturity of hiPSC derived CMs [50]. Despite this limitation, cells with the P710R mutation produce significantly greater force even after normalizing for the increase in cell area (**Figure 4**). There was significant variability in force production within the cell populations, which may be due in part to differences in myofibril density between cells, as suggested by or modeling analysis. The P710R mutation caused significant perturbation in alignment of myofibrils in the mutant cells, a well described phenotype in HCM [51], as well as an increase in the thickness of the z-disc (**Figure 5**). Increased z-disc thickness has been described in many cardiomyopathies [52-54], and we confirmed this phenotype in human myectomy samples from patients with HCM (data not shown), which suggests that z-disc thickening is a conserved phenotype associated with hypercontractility and hypertrophic remodeling. Finally, we observed cellular hypertrophy which was mediated in part by Akt and ERK. ERK activation has been specifically linked to concentric hypertrophy in response to an increase in force index (force production

bioRxiv preprint doi: https://doi.org/10.1101/2020.11.10.375493; this version posted November 10, 2020. The copyright holder for this preprint (which was not certified by peer review) is the author/funder. All rights reserved. No reuse allowed without permission.

integrated over time of contraction) [55]. By comparing cellular responses to an isogenic control, we have more confidence that the altered biomechanical consequences of the P710R mutation are driving both hypercontractility and additional cellular dysfunction.

The P710R mutation induces a number of profound changes to myosin activity whose effects become easier to interpret when integrated into a computational model. Even with similar driving calcium transients and identical rates of thin filament activation by calcium, the model simulations predict a increase in thin filament activation and a lengthening of contraction time resulting solely from the changes in myosin kinetics (specifically the change in regulation of SRX). In simulations where only step size, attachment and detachment rates were changed (as is true for the sS1 construct), there were minimal effects on actin availability (±15% change), which matches the observed similarity in pCa_{50} in sS1 motility with or without the mutation. When the disruption of SRX caused by the mutation is included, the predicted percentage of actin kept in the active state by myosin increases by 8-10 fold. The model used in this study, while by no means comprehensive, provides valuable insights into the expected individual and combined effects of changes to myosin kinetics and biomechanical function on force production, actin activation, and potential sources of variability.

Several important limitations of this project should be addressed. Measurements of the SRX state using shortened constructs that do not contain the full thick filament backbone do not take into account the likely additional stabilization of the SRX in thick filaments *in vivo* (see additional discussion in sup). Hypertrophy measurements and assessment of protein activation were performed on unpatterened cells grown on tissue culture plastic or glass because it would be difficult to quantify phosphorylation in small populations of cells recovered from patterned gel platforms. This modeling work shows the singular effects of a mutation, but does not fully capture potential synergistic or emergent consequences of a mixture of control and mutant myosins acting together. Furthermore, this modeling approach assumes that muscle force is felt uniformly throughout the muscle, while in reality, the spatial distribution of myosins within a sarcomere can have profound effects on the force experienced by individual myosin heads. Future modeling could incorporate spatially explicit information that could provide even more detail on the effects of local loads and heterotypic myosin effects.

In summary, the P710R mutation reduces several functional parameters of the isolated myosin molecule, however, the dysregulation of the SRX state appears to be the major driver of hypercontractility. When expressed as a heterozygous mutation in human stem cell derived cardiomyocytes, this mutation causes hypercontractility, myofibril disruption, and hypertrophy mediated in part through ERK and Akt. This project also demonstrates the substantial benefit of computational modeling integrated with multiscale measurements to give insights into the interactions of dynamic, load-sensitive, functional parameters, and a platform for integrated testing of myosin variants and new drug screening.

bioRxiv preprint doi: https://doi.org/10.1101/2020.11.10.375493; this version posted November 10, 2020. The copyright holder for this preprint (which was not certified by peer review) is the author/funder. All rights reserved. No reuse allowed without permission.

Materials and Methods

Expression and purification of proteins

Recombinant human β-cardiac myosin protein constructs – short motor domain (sS1), short-tailed (2-hep) and long-tailed (25-hep) – were coexpressed with a FLAG-tagged human essential light chain (ELC) in mouse myoblast cells (C2C12) using adenoviral vectors. The sS1 constructs had either a C-terminal enhanced green fluorescent protein ("sS1-eGFP") or a C-terminal eight-residue PDZ-binding peptide ("sS1-AC"). The sS1 constructs were purified with a FLAG affinity and ion-exchange chromatography as previously described [56]. The 2-hep and 25-hep constructs had both an eGFP and PDZ tag on their C-termini. For these longer constructs, human RLC was exchanged for the endogenous mouse RLC while bound to a FLAG resin, and then the myosin was purified as previously described [8].

Actin was prepared as described previously [57] from bovine cardiac muscle (the sequences are identical between bovine and human actin). The actin was dialyzed in ATPase buffer (5 mM KCl, 1 mM DTT, 3 mM $MgCl_2$ and 10 mM imidazole) to form F-Actin for ATPase assays.

Deadheading myosin

Myosin protein used for unloaded motility experiments was further subjected to a 'deadheading' procedure to remove inactive heads. Myosin was mixed with 10x excess of unlabeled F-actin on ice for 5 min, followed by addition of 2 mM ATP for 3 min, then centrifuged at 95 krpm in a TLA-100 rotor (Beckman Coulter) at 4 °C for 20 min. The supernatant was collected. We found that the P710R protein had more inactive heads than WT, as seen in a greater percentage of stuck filaments (5-15%) even after deadheading two times. In contrast, percent stuck filament was 0-5% for WT sS1-AC with or without deadheading. Note, however, that these stuck filament percentages do not directly translate to the percentage of inactive heads; only a very small amount of inactive heads (probably 1% or less) is needed to produce a much larger amount of stuck filaments. For RTF motility experiments, we forgoed deadheading because it did not substantially reduce percent stuck filaments, as 5-15% remained. This is likely because deadheading cannot remove 100% of completely or partially inactive heads.

Single-molecule measurements of load-dependent detachment rates with dual-beam optical trap

The load-dependent detachment rates of WT and P710R sS1-eGFP molecules were measured in a dual-beam optical trap using the harmonic force spectroscopy (HFS) method previously described [10, 11, 58] with slight modifications. The sample chamber consisted of two double-sided tapes between a glass slide and a coverslip spin-coated with 1.6-um-diameter silica beads (Bang Laboratories) and a solution of 0.1%

bioRxiv preprint doi: https://doi.org/10.1101/2020.11.10.375493; this version posted November 10, 2020. The copyright holder for this preprint (which was not certified by peer review) is the author/funder. All rights reserved. No reuse allowed without permission.

nitrocellulose/0.1% collodion in amyl acetate. Experiments were done at 23 °C. The following solutions were flowed into the chamber sequentially, each with a couple minutes of incubation: 1. GFP antibody (Abcam ab1218) diluted to 1 nM in assay buffer (AB; 25 mM imidazole pH 7.5, 25 mM KCl, 4 mM $MgCl_2$, 1 mM EGTA, and 10 mM DTT). 2. BSA diluted to 1 mg/mL in AB (ABBSA), to wash and block the surface. 3. Human β-cardiac myosin sS1-eGFP diluted to 10-50 nM in ABBSA, to bind all the GFP antibodies on the surface. 4. ABBSA, to wash. 5. A final solution consisting of 2 mM ATP, 0.3 nM TMR-phalloidin-labeled biotinylated actin (Cytoskeleton) filaments, an oxygen-scavenging system (0.4% glucose, 0.11 mg/mL glucose oxidase, and 0.018 mg/mL catalase), and 1-um-diameter NeutrAvidin-coated polystyrene beads (ThermoFisher) or 1-um-diameter streptavidin-coated polystyrene beads (Bang Laboratories) diluted in ABBSA. The chamber was sealed with vacuum grease and used for up to 2 hr.

The stiffnesses of the two traps were calibrated using the power spectrum method with corrections for filters, aliasing, and surface effects [59], and were 0.08-0.10 pN/nm for both traps in these experiments. After calibration, a “dumbbell” was made by stretching an actin filament between the two trapped beads (Figure S1). While the stage oscillated at 200 Hz, the dumbbell was lowered near platform beads on the surface to test for binding to a potential myosin. Robust interactions with myosin were indicated by consistent, large, brief displacements of the trapped beads due to stronger association with the oscillating stage. We typically explored ~4-10 platform beads before robust interactions were observed, suggesting that the GFP antibody concentration used resulted in sufficiently low numbers of properly oriented molecules on the surface for single molecule conditions. Time traces were saved and automatically processed as previously described [10, 11]. Briefly, events were selected based on a simultaneous increase in oscillation amplitude and decrease in phase between each bead and the stage. The detachment rate at each force was determined by a maximum likelihood estimation from the durations of events within the force bin. The rates at different forces were then fitted to Eqn. 1 to obtain the two parameters k_0 and δ. The data on multiple molecules presented in this paper are from multiple dumbbells in independent experiments from multiple days.

The step sizes of myosins were determined from the same HFS data by adapting the ensemble averaging method [60] to HFS’s oscillatory data. For each molecule, position traces of all events were aligned at the start of binding, extended to the length of the longest event, and averaged. Then the oscillations were removed by subtracting a fitted sine function. The total step size for each molecule was taken as the difference between the initial position and the end position of the extended, averaged, sine-subtracted traces.

bioRxiv preprint doi: https://doi.org/10.1101/2020.11.10.375493; this version posted November 10, 2020. The copyright holder for this preprint (which was not certified by peer review) is the author/funder. All rights reserved. No reuse allowed without permission.

In vitro motility assays

Motility measurements of WT and P710R sS1-AC used our previously described motility assay [19, 61] with some modifications. Multi-channel flow chambers consisted of double-sided tapes between a glass slide and a coverslip pre-coated with a solution of 0.1% nitrocellulose/0.1% collodion in amyl acetate.

For unloaded motility, the following solutions were flowed into the chamber sequentially: 1. SNAP-PDZ18 (purified as described in Aksel Cell Reports 2015 [19]) diluted to 3 uM in assay buffer (AB; 25 mM imidazole pH 7.5, 25 mM KCl, 4 mM $MgCl_2$, 1 mM EGTA, and 10 mM DTT), incubated for 2 min. 2. BSA diluted to 1 mg/mL in AB (ABBSA), incubated for 2 min. 3. Human β-cardiac sS1-AC diluted to ~200 nM in ABBSA, flowed twice with 2 min incubation each time. 4. ABBSA. 5. A final solution consisting of 2 mM ATP, 2.5 nM TMR-phalloidin-labeled actin filaments, and an oxygen-scavenging system (0.4% glucose, 0.11 mg/mL glucose oxidase, and 0.018 mg/mL catalase) in ABBSA. pH of the final solution was measured to be 7.5 at 23 °C.

For RTF motility, a full pCa curve was generated by one slide with 6-7 channels. The following solutions were flowed into the channels sequentially: 1. SNAP-PDZ18 diluted to 3 uM in AB, incubated for 2 min. 2. ABBSA, incubated for 2 min. 3. Human β-cardiac sS1-AC diluted to 400-600 nM in ABBSA, flowed twice with 2 min. incubation each time. 4. ABBSA. 5. TMR-phalloidin-labeled actin filaments diluted to 10 nM in ABBSA, incubated for 1 min. 6. ABBSA. 7. A final solution consisting of 2 mM ATP, an oxygen-scavenging system (0.4% glucose, 0.11 mg/mL glucose oxidase, and 0.018 mg/mL catalase), 100 nM human troponin complex (expressed, purified, and complex formed as described in Sommese PloS One 2013 [56]), 100 nM bovine cardiac tropomyosin (purified as described in Sommese PloS One 2013 [56]), and varying amounts of $CaCl_2$ (as calculated in [62]) in ABBSA. pH of the final solution was measured to be 7.5 at 23 °C. Troponin and tropomyosin were added only in the final solution because we found that filaments were decorated with the regulatory proteins very quickly and certainly by the time the channels were imaged.

The slide was then placed on a Nikon Ti-E inverted microscope with a 100x TIRF objective. Images were taken for 30 sec at 2 Hz with 300 ms exposure on an Andor iXon+EMCCD camera. Three movies were recorded for each channel. The objective temperature was maintained at 23 +- 0.3 °C as closely as possible to minimize variations in velocities stemming from myosin's high sensitivity to temperature. Movies of all channels on each slide were acquired as quickly as possible, within ~15 min after flowing in the final buffer for the 6-7 channel slides. Despite our foregoing an ATP regeneration system, no slowing down of actin filaments was observed throughout imaging, nor any differences observed with or without an ATP regeneration system.

Movies were processed by FAST (Fast Automated Spud Trekker) for filament tracking and velocity analysis [19]. The following parameters were used in FAST: window size n = 5, path length p = 10, percent tolerance pt = 80, and minimum velocity for stuck

bioRxiv preprint doi: https://doi.org/10.1101/2020.11.10.375493; this version posted November 10, 2020. The copyright holder for this preprint (which was not certified by peer review) is the author/funder. All rights reserved. No reuse allowed without permission.

classification minv = 20 nm/s. All velocities reported in the main text are the mean velocities including stuck filaments (MVIS), which is equivalent, up to a multiplicative factor, to the "percent time mobile" metric defined previously [19]. The lower minv value and higher pt value as used here are appropriate for analyzing loaded or RTF motility data. While a higher minv (80, as used in some previous publications) and lower pt (20 in some previous publications) are more appropriate for analysis of unloaded motility data (along with reporting "Top5%" or "MVEL-filtered" velocities), we used the same set of FAST parameters to analyze all motility data reported in this paper so that values can be directly compared.

The Hill equation was fitted for each independent experiment producing MVIS values at 6-7 pCa concentrations (6-7 channels). Variation among the three movies taken for any particular channel was very minimal and smaller than variation between independent slides/experiments. Therefore, to capture the true experimental or biological variation, 4-5 independent experiments (slides) were performed for both WT and P710R. Error bars on data points at each pCa value represent s.e.m. of all independent experiments. Similarly, error bars on the fitted pCa50 and n values represent s.e.m. of the various fitted values from independent experiments.

Actin-activated ATPase assay

NADH-coupled ATPases were used to compare the activity of the 2-hep and 25-hep constructs of WT and P710R β-cardiac myosin as previously described [63]. Briefly, actin was prepared as described in [57] and dialyzed 4x into ATPase reaction buffer without ATP: 5 mM KCl, 10 mM imidazole pH 7.5, 3 mM $MgCl_2$, and 1 mM DTT. Gelsolin was prepared as previously described [64] and added to the actin at a final molar ratio of ~1:200. In a 96-well plate, actin was mixed with ATPase reaction buffer to achieve final concentrations of 1-100 uM, and myosin was added at a final concentration of 0.025 uM. To measure the basal rate without actin, myosin was added to ATPase reaction buffer at final concentrations of 0.075 – 0.125 uM. To initiate the reaction, a 5x coupling solution containing 100 U/mL lactate dehydrogenase (Sigma L1254), 500 U/mL pyruvate kinase (Lee Biosolutions 500-20), 2.5 mM phospho(enol) pyruvate (Sigma P0564), 10 mM ATP, and 2 mM NADH (Sigma N8129) was added at 1/5 the volume of the final reaction. The plate was shaken for 5 minutes at 23°C before reading at 340 nm every 30 seconds for 25 minutes. A standard curve of ADP from 0 – 300 uM was created to convert the absorbance values to concentration of ADP produced.

Fitting the data to the Michaelis-Menten equation using the curve fitting feature in MATLAB or the non-linear fit feature in PRISM allowed for calculation of the maximum actin-activated ATPase activity rate (k_{cat}) and Michaelis-Menten constant (K_M) (Table S1 and Figure S4). Curves were normalized to the k_{cat} of the 2-hep myosin. Presented data combine the results from triplicate measurements of each of two independent protein preparations on separate days.

bioRxiv preprint doi: https://doi.org/10.1101/2020.11.10.375493; this version posted November 10, 2020. The copyright holder for this preprint (which was not certified by peer review) is the author/funder. All rights reserved. No reuse allowed without permission.

Mant-ATP single turnover assay

Single turnover experiments were performed as previously described [8, 13], using WT and mutant versions of human ß-cardiac 2-hep and 25-hep. These experiments were performed in a 96-well plate by mixing 200 nM myosin in a buffer (10 mM Tris pH 7.5, 4 mM $MgCl_2$, 1 mM EDTA, 1 mM DTT, 5 mM potassium acetate) with 2′-(or-3′)-*O*-(*N*-Methylanthraniloyl) adenosine 5′-triphosphate (mant-ATP, Thermo Fischer Scientific) to a final concentration of 200-240 nM. ~10 s after mixing myosin and mantATP buffer, 2 mM ATP was added and the fluorescent signal (470 nm Em/405 nm Ex) was measured every ~2 s for 16 min. The traces were normalized, plotted, and fit to a five parameter bi-exponential decay function to yield rates and amplitudes of fast (DRX) and slow (SRX) phases (Table S1).

CRISPR/Cas9 based editing of hiPSCs

The control human iPSC line (Stanford Cardiovascular Institute [SCVI-113]) was obtained from the Stanford CVI iPSC Biobank. These cells were acquired, reprogrammed and deidentified in accordance with approved IRB protocols and cultured in the appropriate media to maintain stemness. The iPSCs were maintained in defined E8 media (Gibco) on tissue culture plates coated with Matrigel (Corning) diluted 1:100 in DMEM/F12 at 37°C in 5% CO_2. The P710R mutation was edited into these cells using a method that has been described previously [65, 66]. We designed a guide RNA (GCTGCGCTGCAATGGTGTGCTGG) that was predicted to be highly specific to a site 34 basepairs upstream of the desired mutation site and cloned it into the pSpCas9 (BB) 2A-GFP (PX458) plasmid. We also designed 500 basepair homology regions surrounding our cut site and including a C->G mutation at basepair 9699 to encode the P->R transition and a silent mutation to form a TTAA site at 9647-9650. These homology regions were cloned into an MV-Puro-TK plasmid surrounding a Puromycin resistance – TK selection cassette and both plasmids were introduced into the control iPSCs using Lipofectamine 3000. Puromycin was used to select for positively edited cells and then the Transposagen X reagent was used to excise the cassette leaving "scarless" silent TTAA mutation and Ganciclovir was used to select for successfully repaired cells. Sequencing confirmed correct, single allele edits with no indels or other mutations on the second allele of MYH7 or on MYH6 (a close homologue in this region).

Cardiomyocyte differentiation and culturing of hiPSCs

Cells were differentiated into the cardiac lineage following a well established protocol that relies on sequential activation and inhibition of the Wnt pathway. Specifically, we began differentiation when the cells reached ~75% confluence in RPMI media with B27 minus insulin supplement and 5 µM Chir-99021. After 24 hours, the media was replaced or supplemented with RPMI media with B27 minus insulin supplement, and then at 48 hours, the media was replaced by RPMI media with B27 minus insulin supplement

bioRxiv preprint doi: https://doi.org/10.1101/2020.11.10.375493; this version posted November 10, 2020. The copyright holder for this preprint (which was not certified by peer review) is the author/funder. All rights reserved. No reuse allowed without permission.

plus 5 µM IWR or 2 µM C59. On the fourth day after the start of differentiation, the media was replaced with RPMI media with B27 minus insulin supplement, and on the sixth day, the media was replaced with RPMI media with B27. Glucose starvation in glucose free RPMI with B27 was performed after the onset of beating for 4 days, and cells were replated before day 20 to allow for firm attachment to a fresh Matrigel coated plate. Cells were maintained in RPMI media with B27 for up to 60 days. Calcium transients were captured using a wide-field fluorescent camera on cells loaded with Fluo4 dye after 30 minutes using a point electrode and 1Hz pacing. Linear regions of interest approximately the length of 2-5 cells were chosen perpendicular to the direction of conduction at 4 different sites at least 2 mm apart. Transients were normalized to their baseline and the time to 90% of peak, time over 90%, and decay from 90% of peak to 5% above baseline times were measured and found to be not significantly different between control and mutant cells (Figure S8).

Micropatterning hydrogels and substrates for microscopy

Micropatterned hydrogels gels were created as previously described. SU-8 photolithography was used to create molds for stamps with rectangular features 10 µm deep with a 7:1 aspect ratio and an area of 2500 μm^2. These single cell patterns were arranged in a 1 cm by 1 cm grid, spaced to minimize the risk of mechanical interaction between adjacent cells. The area of these patterns was also larger than the median and 75 quartile of the cell spread area for both control and P710R cells, so it allowed for assessment of cell area with a spatial cue. Polydimethylsiloxane (PDMS) was mixed at a 9:1 by weight ratio of elastomeric base to primer and curing agent, mixed, degassed, and cured at 65°C for a hour. The PDMS stamps were coated in a 10:1 dilution of Matrigel in L15 media overnight at 4°C, rinsed in media and gently dried with Nitrogen. Stamps were then inverted and pressed onto cleaned and plasma-treated glass coverslips or Aclar film and weighted with a 50g mass for at least 3 minutes to ensure even pressure and coverage.

For creation of micropatterned hydrogels, a mixture of Acrylamide, Bisacrylamide, HEPES and 0.5 µm fluorescent beads (Life Technologies, FluoSpheres) when used for traction force microscopy and polymerized with TEMED and 10% APS according to a formula which has been validated to produce gels of a stiffness of 10 kPa. This stiffness matches the physiologic stiffness of healthy myocardium near the beginning stages of disease.

Traction force microscopy and calculation

Single cell traction forces were assessed from single cells using algorithms described in our previous publications. We used both a Leica live cell imaging scope with a Prime 95 camera and a Nikon TiE microscope with an Andor Neo sCMOS camera. Cells were imaged in the bright-field to determine cell area and screen for beating,

bioRxiv preprint doi: https://doi.org/10.1101/2020.11.10.375493; this version posted November 10, 2020. The copyright holder for this preprint (which was not certified by peer review) is the author/funder. All rights reserved. No reuse allowed without permission.

apparently single cells. Videos were then collected in the bright field and fluorescent channels to capture at least two full cardiac contraction cycles, at a minimum of 25 frames per second using a 40x 0.85NA or 20x air objective.

Electrical field stimulation of 10V/cm at a frequency of 1 Hz was imposed with a carbon electrode throughout the acquisition of videos, and only cells that were able to keep up with 1 Hz pacing were included in further analysis. Our custom script and user interface in MATLAB allows for measurement of the cell outline and outputs the normalized displacements, total traction force, contraction time, moments, and integrated contraction impulse (force integrated over the time of contraction).

Immunostaining and electron microscopy

At day 45 after differentiation, the cells were replated on 48-well tissue culture plastic, hydrogels or micropatterned aclar film and allowed to attach and grow for 4 or 7 days before fixing for further imaging. For immunostaining to determine cell size, cells were plated sparsely on a 48 well plate and allowed to attach for 4 days, and then fixed in 4% paraformaldehyde and permeabilized with 0.1% triton. Cells were blocked in 5% BSA, stained with 1:200 cTnT primary antibody (Abcam:ab45932) and a 1:500 dilution of the 488 anti-rabbit antibody, stained with DAPI, and imaged on the Keyence microscope. Cell area was quantified with imageJ and Cell Profiler [67] and statistical differences in cell size were assessed with a non-parametric Mann-Whitney test in PRISM.

For assessment of α- and β-myosin expression, cells were fixed and permeabilized in 4% PFA and 0.05% triton for fifteen minutes, blocked in a goat serum solution for one hour, and incubated in 1:50 β myosin mouse primary antibody, 1:100 α myosin rabbit primary antibody overnight at 4°C. Secondary antibodies Goat anti mouse 488 and Goat anti rabbit 647 were used to visualize and quantify the proteins.

For electron microscopy, cells were grown on microcontact printed Aclar film for 1 week and the fixed with a mixture of 2% glutaraldehyde (EMS Ca# 16000) and 4% Formaldehyde (EMS Cat # 15700) in 0.1M Sodium Cacodylate (EMS Cat# 12300) pH 7.4 for 1 hr. The fixing solution was replaced with 1% Osmium tetroxide (EMS Cat# 19100) for 2 hours at room temperature, washed 3x with ultra-filtered water, then stained in 1% Uranyl Acetate at RT for 2 hours. Samples were dehydrated in a series of ethanol washes (50%, 70%, 95%, 100%) for 30 min. each. The samples were transferred to Propylene Oxide (PO) and then infiltrated with Embed-812 resin (EMS Cat#14120) with PO at 1:2, 1:1 and 2:1 ratios for 2 hours and then placed in resin for 2 hours and placed in 65°C oven overnight. Thin sections (80 nm) were cut along a plane parallel to the patterned substrate plane of the cell (near the plane of attachment) using a Leica EM UC7 Ultramicrotome and placed on 100 mesh coper grids (EMS). Samples were post-stained with 1.5% Uranyl Acetate in 50% Acetone for 30 seconds, then washed, dried, and then stained for 2 minutes in Sato's lead cirtrate and imaged with a JEM-1400 transmission electron microscope (JEOL) at 120 kV. Between 5 and 10 images were taken between

bioRxiv preprint doi: https://doi.org/10.1101/2020.11.10.375493; this version posted November 10, 2020. The copyright holder for this preprint (which was not certified by peer review) is the author/funder. All rights reserved. No reuse allowed without permission.

2500X and 3000X magnification with a on Gatan Orius 832 digital camera (Gatan, Pleasanton, CA) and sarcomere length and z-disk thickness was quantified in image J.

Inhibitor study

To clarify the effect of ERK and Akt, the cells were treated with either Akt inhibitor (Akti 1/2, Tocris: 5µM) or and ERK inhibitor (SCH772984, SelleckChem: 1µM) every 3 days between day 26 and day 46 (a time frame over which hiPSC-CMs have been shown to increase in area). At day 46, the cells were replated sparsely at a density of 50 thousand cells per coverslip and fixed and stained for β-myosin heavy chain and cardiac troponin T (Abcam:ab45932). The area of cells was quantified using Cell Profiler and the results from 2 batches of cells were combined and analyzed using Graphpad PRISM software with a 2-way ANOVA and the Kruskal-Wallis non-parametric test for multiple comparisons.

Assessment of protein transcription, expression and activation

Batch-matched cell lysates were collected from nine separate differentiations between day 50 and 60 of differentiation in either RIPA buffer supplemented with protease inhibitor, phosphatase inhibitor, and DNAse for western blot analysis or in TRIZOL LS for transcript analysis. For western blots, to measure both the activation of signaling proteins and the expression of myosin heavy chains, we used a 4-15% gradient gel (BIORAD) and separated at 150 V for 2 hours. Proteins were transferred to a nitrocellulose membrane at 80V for two hours on ice. These membranes were blocked in a 5% milk protein block solution in Tris buffered saline with 0.01% Tween (TBST), rinsed, and incubated overnight at 4 degrees in a 1:1000 solution of primary antibody in 2% BSA. After primary antibody incubation (pERK:Cell Signaling #9106S and pAkt: Cell Signaling #2965S), the gels were rinsed in TBST and incubated in 1:5000 secondary antibodies conjugated with HRP. After a final rinse, the gels were incubated for five minutes in Clarity ECL substrate (BIORAD), imaged on a chemidoc luminescent scanner, and band intensity was quantified in FIJI. After staining for the fluorescent protein, the membranes were stripped in a solution of 15 g glycine, 1 g SDS, 10 mL Tween 20 and distilled water (1L) and reblocked and reincubated in a 1:1000 dilution of primary for the total amount of protein (ERK:Cell Signaling 9102S and Akt: Cell Signaling #9272S). Many of these blots were also stained for α and β myosin antibodies that were developed by the Kraft lab and the Spudich lab. For each differentiation batch, the densitometry of measurements were normalized to the total protein, and then the sample from P710R cells were normalized to the control cells from that batch.

bioRxiv preprint doi: https://doi.org/10.1101/2020.11.10.375493; this version posted November 10, 2020. The copyright holder for this preprint (which was not certified by peer review) is the author/funder. All rights reserved. No reuse allowed without permission.

Computational modeling

We used a previously validated continuum model which incorporates discretized flux equations to describe transitions of myosin heads and thin filaments from inactive to active/bound states and provides prediction of active and passive force [35, 68]. This model also incorporates force-sensitive release of myosin heads from the thick filament and was modified to reflect the asymmetric load-dependent detachment rate (Figure S7). The fraction of binding sites in the active state was defined as N_{on}, and the fraction of binding sites that in the filament overlap zone based on the length of the thick and thin filament and sarcomere length is defined as $N_{overlap}$. The regulation of the thin filament activation is described by the following equation:

$$J_{on} = k_{on}\,[Ca^{2+}]\left(N_{overlap} - N_{on}\right)\left(1 + k_{coop}\left(\frac{N_{on}}{N_{overlap}}\right)\right) \qquad \text{Eqn. 4}$$

J_{on} represents the flux of thin filament binding sites from the off state to the on state and is proportional to the fraction of thin filament binding regions in an available position for binding according to the length of the thin filaments and half sarcomere ($N_{overlap}$) that are not already activated (N_{on}). k_{on} is a rate constant ($M^{-1}\,s^{-1}$) that determines the rate of thin filament activation proportional to the concentration of Ca^{2+}. k_{coop} is a unitless term that describes the interactions between regulatory units on the thin filament that contribute to myofilament cooperativity. N_{bound} is defined as the fraction of binding sites that are currently bound to myosin, and this fraction cannot transition to the off state until after myosin detachment.

$$J_{off} = k_{off}\left(N_{on} - N_{bound}\right)\left(1 + k_{coop}\left(\frac{N_{overlap} - N_{on}}{N_{overlap}}\right)\right) \qquad \text{Eqn. 5}$$

J_{off} represents the flux of thin filament from the on (but unbound) state to the off state and is proportional to the fraction of active binding sites that are not already bound to myosin. The k_{coop} term accelerates the deactivation of the thin filament to reflect that thin filament deactivation is cooperative across the thin filament. The rate constant for thin filament deactivation (k_{off}) was limited to 100-200 s^{-1}.

M_{off}, M_{on}, and $M_{FG,i}$ were defined as the fraction of myosin in the off state (equivalent to SRX), the on state (available but unbound), and force generating states with i=1-41 different displacements (x) between the binding site and the zero load position of the myosin head. The range of potential positions of myosin heads reative to the no-load positions (x_i) range from -10 to 10 nm with a bin size of 0.5 nm. A series of flux equations (J1, J2, J3, and J4) describe the transitions between these myosin states:

bioRxiv preprint doi: https://doi.org/10.1101/2020.11.10.375493; this version posted November 10, 2020. The copyright holder for this preprint (which was not certified by peer review) is the author/funder. All rights reserved. No reuse allowed without permission.

$$J_1 = k_{-SRX}(1 + k_{force} * F_{Total})M_{off} \quad \text{Eqn. 6}$$

J_1 represents the flux of myosin heads from the off state (M_{off}) to the on state (M_{on}) and is proportional to the fraction of heads in the SRX state. Based on previous modeling results and studies of the SRX state in muscle fibers and myofibrils, we assumed that the rate would be increased by increasing force in the muscle and so included a coefficient of force-sensitivity (k_{force}) with units of N^{-1} m^2. The relative increase in the rate (k_{-SRX}) and the baseline and relative k_{force} were fit to the representative traces.

$$J_2 = k_{+SRX} * M_{on} \quad \text{Eqn. 7}$$

J_2 represents the flux of myosin heads from the on but unattached state (M_{on}) to the off state and is proportional to the fraction of heads in the SRX state. The k_{+SRX} rate constant was held unchanged between control and mutant myosin simulations at 200 s^{-1}.

$$J_3(x) = k_A * e^{\frac{-k_{cb}x^2}{2K_BT}} * M_{on}(N_{on} - N_{bound}) \quad \text{Eqn. 8}$$

J_3 represents the flux of myosin heads from the on but unattached state (M_{on}) to the attached, force generating state ($M_{FG,i}$) and is proportional to the fraction of myosin heads in the on state as well as the fraction of active, unbound binding sites on the thin filament. The Gaussian term reflects the probably of a myosin head with spring constant k_{cb} being stretched to length x by thermal energy. k_{cb} is the stiffness of the crossbridge spring and has units of N m^{-1}. K_B is the Boltzmann's constant (1.38E-23 J K^{-1}) and T is the temperature (set to 310 K). The k_A rate constant was derived from our previously reported sS1 ATPase measurements and associated modeling analysis [16] and has units s^{-1}. The values were calculated from the previously published forward attachment rate of myosin (k_A) multiplied by the K_{app} to account for changes in actin affinity and the fractional (unitless) description of actin availability in this model. This scaling of k_A transforms it to units of s^{-1} (compared with the reported units of s^{-1} μM^{-1} [16]). Finally, after calculating this rate constant (k_A) from previously reported values, we divided by the integral of the gaussian term (which depends on k_{cb}) to describe the density of flux at each segment of the available range of binding, making the final units calculated within the model (s^{-1} nm^{-1})consistent with rate constants previously reported using this model [35]).

The final flux equations describe bound myosins exiting the attached state.

$$J_4(x) = k_0 * e^{\frac{-k_{cb}x\delta}{K_BT}} * M_{FG,i}(x_i) \text{ if } |x_i| < 8 \text{ nm, and}$$

bioRxiv preprint doi: https://doi.org/10.1101/2020.11.10.375493; this version posted November 10, 2020. The copyright holder for this preprint (which was not certified by peer review) is the author/funder. All rights reserved. No reuse allowed without permission.

$$J_4(x) = k_0 * e^{\frac{-k_{cb}x\delta}{K_BT}} * M_{FG,i}(x_i) + (|x_i| - 8) * p_{max} \quad \text{Eqn. 9}$$

Where k_0 and δ were taken from HFS measurements and p_{max} is the maximum parameter rate that was set to 5000 s^{-1}. The overall rate of detachment increases towards p_{max} as the displacement of the myosin head relative to its baseline position extends beyond 8 nm based on reported averages for powerstroke ranges and a natural limit for myosin head extension. Adding the muscle force (N/m^2) normalized by the number of myosin heads (1.2E16 m^-2) into the calculation of detachment rate caused only a very small change in the overall fit (less than 10% increase in mean normalized deviation). The highest expected contribution of this normalized force at peak for these cells is less than half than the force of the individual cross bridge springs, so it was not included in these calculations.

These flux expressions are combined into the following differential equations describing the rates of transition between thin filaments and myosin states.

$$\frac{dN_{off}}{dt} = -J_{on} + J_{off} \quad \text{Eqn. 10}$$

$$\frac{dN_{on}}{dt} = J_{on} - J_{off} \quad \text{Eqn. 11}$$

$$\frac{dM_{off}}{dt} = -J_1 + J_2 \quad \text{Eqn. 12}$$

$$\frac{dM_{on}}{dt} = \left(J_1 + \sum_{i=1}^{n} J_{4,x_i}\right) - \left(J_2 + \sum_{i=1}^{n} J_{3,x_i}\right) \quad \text{Eqn. 13}$$

$$\frac{dM_{FG,i}}{dt} = J_{3,x_i} - J_{4,x_i} \quad \text{Eqn. 14}$$

Where i = 1…41

As described above, the force-generating state is further subdivided into 41 potential binding positions, and the binding position determines the load experienced by the myosin head. These equations are calculated at 1 ms intervals. The total force is also calculated at each time and feeds into the calculation of J_1.

$$F_{total} = F_{active} + F_{passive} \quad \text{Eqn. 15}$$

bioRxiv preprint doi: https://doi.org/10.1101/2020.11.10.375493; this version posted November 10, 2020. The copyright holder for this preprint (which was not certified by peer review) is the author/funder. All rights reserved. No reuse allowed without permission.

$$F_{active} = N_0 k_{cb} \sum_{i=1}^{n} M_{FG,i}(x_i + x_{ps}) \quad \text{Eqn. 16}$$

$$F_{passive} = k_p(L - L_0) \quad \text{Eqn. 17}$$

The total force is comprised of active and passive force components. The active force depends on the number of myosins heads in a hypothetical cardiac half-sarcomere with a cross-sectional area of 1 m^2. We also included a series stiffness of 100 N m^{-2} nm^{-1} that has previously been shown to improve model fit to relaxation dynamics [69]. This parameter accounts for serial compliance of the cell and substrate and was adjusted to predict shortening of the sarcomeres within the range of cell shortening we measured for these cells (2-3%) and the percent sarcomere shortening measured in previous studies of hiPSC-CMs with MYH7 mutations [47]. The passive force was determined based on a linear passive stiffness term (k_p), defined as 10 N m^{-2} nm^{-1}, and the change in length from the baseline length (L_0) of 880 nm (to match the sarcomere lengths we measured in these cells). N_0 is the number of myosin heads in a hypothetical cardiac half-sarcomere which was set to 1.2E16 for these simulations. This estimation was derived from the assumptions that there are about 100 myosin heads oriented towards actin per half thick filament [6], the half filaments have a spatial density of 4E14 m^{-2} [70], and the myofibrils in cell occupy ~30% of the cell space (by our observation in electron microscopy images). Multiplying these three numbers together (100 x 4E14 x 0.3) gives an estimate of 1.2E16 for the average myosin head density, but variation in the density of myofibrils or the density of heads on less mature thick filaments might contribute to the variability observed in the cells.

Our measured calcium normalized traces were scaled between pCa 6.17 and 6.72 according to the reported calibrated values from the previously published model simulations [35]. We optimized the value of k_{on}, k_{force}, k_{coop}, k_{cb} and the relative change in k_{-SRX} and k_{force} to find the best fit of $F_{total} - F_{baseline}$ to our representative traces. k_{on} was initially set to 2E7 and was allowed to vary between 1E7 and 1E8. k_{force} was initially set to 2 E-5 and was allowed to vary between 1E-6 and 1E-2. k_{coop} was initially set to 6 and allowed to vary between 4 and 7, and reached the upper bound in this optimization. k_{cb} was originally set to 0.001 and was allowed to vary between 0.01 and 0.0001.The relative rate of k_{-SRX} and k_{force} of the mutant compared to control was originally set to 5 and 1 and allowed to vary between 0 and 20, or 0.1 and 10, respectively. k_{-SRX} for control was set to 20 s^{-1}, based on measurements of the SRX percentage in cell ranging from ~60 to 90% in hiPSC-CMs [47]. After defining a parameter set that fit the WT curve, a specific optimization of the value for k_{-SRX} for the P710R mysoin was performed by initially setting the value of k_{-SRX} to that of the WT myosin (20 s^{-1}) and again allowed to varied between 0 and a 20 fold increase over WT. We also compared the fit to the data after optimizing both k_{-SRX} and kforce or just k_{+SRX} (Figure S9), but found less than 1% improvement in

bioRxiv preprint doi: https://doi.org/10.1101/2020.11.10.375493; this version posted November 10, 2020. The copyright holder for this preprint (which was not certified by peer review) is the author/funder. All rights reserved. No reuse allowed without permission.

the mean normalized deviation (error term defined in previous description of the model [35]).

We also performed sensitivity analysis to determine the effect of each parameter on the active force and the %SRX at peak contraction (Figure S11). While holding the rest of the parameters constant at the best fit values, we varied one parameter to 0.1, 0.5, 2 and 10 times its original value and plotted the results.

Statistical analysis

In general, p-values were calculated from a student t-test or a mann-whitney test if the distribution failed to pass a series of tests for normal distribution (Anderson-Darling, D'Agostino & Pearson, and Shapiro Wilk) with thresholds of $p < 0.05$.

Acknowledgements

This work was funded by NIH grants RM1GM33289 to JAS, DB, BLP; 1R21HL13099301 to DB and BLP; HL117138 to JAS; HL123655 to DB; and HL133359 and HL149164 to KSC. It was also funded by American Heart Association grants 17CSA33590101 to BLP and DB; and American Heart Association Postdoctoral Fellowship (20POST35211011) to ASVR. ASVR and KBK were supported by NIH T32 HL094274. M.M.M. was supported by the Stanford Cellular and Molecular Biology training grant. GP was supported by the Swiss National Science Foundation (SNSF) Early Postdoc Mobility Fellowship (#P2SKP2_164954). This work was also supported by NIH S10RR026775. The human iPSC line(s) were obtained from Joseph C. Wu, MD, PhD at the Stanford Cardiovascular Institute funded by NIH 75N92020D00019. We also acknowledge John Perrino and the electron microscopy imaging core for their help with fixing, sectioning and imaging of the cell samples. We acknowledge Alexandre Ribeiro for his initial help with micropatterning experiments and Arjun Adhikari for his preliminary work on the molecular data. We also acknowledge a generous gift of an α myosin antibody from Theresia Kraft, and we acknowledge Oscar Abilez for his help with imaging calcium transients.

Author Contributions

AVR performed and analyzed the functional measurements of the hiPSC-CMs (TFM, immunostaining, inhibitor treatment) and performed computational modeling. CL developed techniques and performed and analyzed the HFS and motility measurements. KBK performed the initial gene editing of the cells and assisted with preliminary molecular and cellular measurements. MMM performed and analyzed the 2-hep and 25-hep ATPase and single-turnover measurements. CL, MMM, and DS prepared protein. DS performed preliminary motility measurements. GP wrote the code for analysis of the TFM

bioRxiv preprint doi: https://doi.org/10.1101/2020.11.10.375493; this version posted November 10, 2020. The copyright holder for this preprint (which was not certified by peer review) is the author/funder. All rights reserved. No reuse allowed without permission.

data. GJ contributed to the quantification of cell hypertrophy. GJ, SR, GF, and MZ assisted with functional measurements of hiPSC-CMs. AJ contributed to the sensitivity analysis and optimization of the modeling results. KSC assisted with the adaptation of the modeling platform to this project. KMR and AD prepared the transgenic virus. AVR, CL, and MMM wrote the manuscript. BLP, KMR, JAS, and DB contributed to intellectual oversight of the project and writing the manuscript. All authors contributed intellectually to discussions of the results and reviewed and edited the paper.

References

1. Virani, S.S., et al., *Heart Disease and Stroke Statistics-2020 Update: A Report From the American Heart Association.* Circulation, 2020. **141**(9): p. e139-e596.
2. Semsarian, C., et al., *New perspectives on the prevalence of hypertrophic cardiomyopathy.* J Am Coll Cardiol, 2015. **65**(12): p. 1249-1254.
3. Jorda, P. and A. Garcia-Alvarez, *Hypertrophic cardiomyopathy: Sudden cardiac death risk stratification in adults.* Glob Cardiol Sci Pract, 2018. **2018**(3): p. 25.
4. Arad, M., J.G. Seidman, and C.E. Seidman, *Phenotypic diversity in hypertrophic cardiomyopathy.* Hum Mol Genet, 2002. **11**(20): p. 2499-506.
5. Ho, C.Y., et al., *Genotype and Lifetime Burden of Disease in Hypertrophic Cardiomyopathy: Insights from the Sarcomeric Human Cardiomyopathy Registry (SHaRe).* Circulation, 2018. **138**(14): p. 1387-1398.
6. Spudich, J.A., *Hypertrophic and dilated cardiomyopathy: four decades of basic research on muscle lead to potential therapeutic approaches to these devastating genetic diseases.* Biophys J, 2014. **106**(6): p. 1236-49.
7. Adhikari, A.S., et al., *Early-Onset Hypertrophic Cardiomyopathy Mutations Significantly Increase the Velocity, Force, and Actin-Activated ATPase Activity of Human beta-Cardiac Myosin.* Cell Rep, 2016. **17**(11): p. 2857-2864.
8. Adhikari, A.S., et al., *beta-Cardiac myosin hypertrophic cardiomyopathy mutations release sequestered heads and increase enzymatic activity.* Nat Commun, 2019. **10**(1): p. 2685.
9. Kawana, M., et al., *Biophysical properties of human beta-cardiac myosin with converter mutations that cause hypertrophic cardiomyopathy.* Sci Adv, 2017. **3**(2): p. e1601959.
10. Liu, C., et al., *Controlling load-dependent kinetics of beta-cardiac myosin at the single-molecule level.* Nat Struct Mol Biol, 2018. **25**(6): p. 505-514.
11. Sung, J., et al., *Harmonic force spectroscopy measures load-dependent kinetics of individual human beta-cardiac myosin molecules.* Nat Commun, 2015. **6**: p. 7931.
12. Hooijman, P., M.A. Stewart, and R. Cooke, *A new state of cardiac myosin with very slow ATP turnover: a potential cardioprotective mechanism in the heart.* Biophys J, 2011. **100**(8): p. 1969-76.
13. Anderson, R.L., et al., *Deciphering the super relaxed state of human beta-cardiac myosin and the mode of action of mavacamten from myosin molecules to muscle fibers.* Proc Natl Acad Sci U S A, 2018. **115**(35): p. E8143-E8152.

bioRxiv preprint doi: https://doi.org/10.1101/2020.11.10.375493; this version posted November 10, 2020. The copyright holder for this preprint (which was not certified by peer review) is the author/funder. All rights reserved. No reuse allowed without permission.

14. Sarkar, S.S., et al., *The hypertrophic cardiomyopathy mutations R403Q and R663H increase the number of myosin heads available to interact with actin.* Sci Adv, 2020. **6**(14): p. eaax0069.
15. Kaski, J.P., et al., *Prevalence of sarcomere protein gene mutations in preadolescent children with hypertrophic cardiomyopathy.* Circ Cardiovasc Genet, 2009. **2**(5): p. 436-41.
16. Vera, C.D., et al., *Myosin motor domains carrying mutations implicated in early or late onset hypertrophic cardiomyopathy have similar properties.* J Biol Chem, 2019. **294**(46): p. 17451-17462.
17. Milani-Nejad, N. and P.M. Janssen, *Small and large animal models in cardiac contraction research: advantages and disadvantages.* Pharmacol Ther, 2014. **141**(3): p. 235-49.
18. Schroer, A., et al., *Engineering hiPSC cardiomyocyte in vitro model systems for functional and structural assessment.* Prog Biophys Mol Biol, 2019. **144**: p. 3-15.
19. Aksel, T., et al., *Ensemble force changes that result from human cardiac myosin mutations and a small-molecule effector.* Cell Rep, 2015. **11**(6): p. 910-920.
20. Yang, X., L. Pabon, and C.E. Murry, *Engineering adolescence: maturation of human pluripotent stem cell-derived cardiomyocytes.* Circ Res, 2014. **114**(3): p. 511-23.
21. Karakikes, I., V. Termglinchan, and J.C. Wu, *Human-induced pluripotent stem cell models of inherited cardiomyopathies.* Curr Opin Cardiol, 2014. **29**(3): p. 214-9.
22. Ribeiro, A.J., et al., *Contractility of single cardiomyocytes differentiated from pluripotent stem cells depends on physiological shape and substrate stiffness.* Proc Natl Acad Sci U S A, 2015. **112**(41): p. 12705-10.
23. Jung, G., et al., *Time-dependent evolution of functional vs. remodeling signaling in induced pluripotent stem cell-derived cardiomyocytes and induced maturation with biomechanical stimulation.* FASEB J, 2016. **30**(4): p. 1464-79.
24. Ribeiro, A.J.S., et al., *Multi-Imaging Method to Assay the Contractile Mechanical Output of Micropatterned Human iPSC-Derived Cardiac Myocytes.* Circ Res, 2017. **120**(10): p. 1572-1583.
25. Campbell, K.S., *Compliance Accelerates Relaxation in Muscle by Allowing Myosin Heads to Move Relative to Actin.* Biophys J, 2016. **110**(3): p. 661-668.
26. Campbell, S.G., P.C. Hatfield, and K.S. Campbell, *A mathematical model of muscle containing heterogeneous half-sarcomeres exhibits residual force enhancement.* PLoS Comput Biol, 2011. **7**(9): p. e1002156.
27. Powers, J.D., et al., *A Spatially Explicit Model Shows How Titin Stiffness Modulates Muscle Mechanics and Energetics.* Integr Comp Biol, 2018. **58**(2): p. 186-193.
28. Tanner, B.C., T.L. Daniel, and M. Regnier, *Filament compliance influences cooperative activation of thin filaments and the dynamics of force production in skeletal muscle.* PLoS Comput Biol, 2012. **8**(5): p. e1002506.
29. Tanner, B.C., T.L. Daniel, and M. Regnier, *Sarcomere lattice geometry influences cooperative myosin binding in muscle.* PLoS Comput Biol, 2007. **3**(7): p. e115.

bioRxiv preprint doi: https://doi.org/10.1101/2020.11.10.375493; this version posted November 10, 2020. The copyright holder for this preprint (which was not certified by peer review) is the author/funder. All rights reserved. No reuse allowed without permission.

30. Williams, C.D., M. Regnier, and T.L. Daniel, *Elastic energy storage and radial forces in the myofilament lattice depend on sarcomere length.* PLoS Comput Biol, 2012. **8**(11): p. e1002770.
31. Williams, C.D., M. Regnier, and T.L. Daniel, *Axial and radial forces of cross-bridges depend on lattice spacing.* PLoS Comput Biol, 2010. **6**(12): p. e1001018.
32. Williams, C.D., et al., *The length-tension curve in muscle depends on lattice spacing.* Proc Biol Sci, 2013. **280**(1766): p. 20130697.
33. Aboelkassem, Y., et al., *Contributions of Ca2+-Independent Thin Filament Activation to Cardiac Muscle Function.* Biophys J, 2015. **109**(10): p. 2101-12.
34. Barrick, S.K., et al., *Computational Tool to Study Perturbations in Muscle Regulation and Its Application to Heart Disease.* Biophys J, 2019. **116**(12): p. 2246-2252.
35. Campbell, K.S., P.M.L. Janssen, and S.G. Campbell, *Force-Dependent Recruitment from the Myosin Off State Contributes to Length-Dependent Activation.* Biophys J, 2018. **115**(3): p. 543-553.
36. Greenberg, M.J., H. Shuman, and E.M. Ostap, *Inherent force-dependent properties of beta-cardiac myosin contribute to the force-velocity relationship of cardiac muscle.* Biophys J, 2014. **107**(12): p. L41-L44.
37. Woody, M.S., et al., *Positive cardiac inotrope omecamtiv mecarbil activates muscle despite suppressing the myosin working stroke.* Nat Commun, 2018. **9**(1): p. 3838.
38. McKillop, D.F. and M.A. Geeves, *Regulation of the interaction between actin and myosin subfragment 1: evidence for three states of the thin filament.* Biophys J, 1993. **65**(2): p. 693-701.
39. Bremel, R.D. and A. Weber, *Cooperation within actin filament in vertebrate skeletal muscle.* Nat New Biol, 1972. **238**(82): p. 97-101.
40. Kad, N.M., et al., *Single-myosin crossbridge interactions with actin filaments regulated by troponin-tropomyosin.* Proc Natl Acad Sci U S A, 2005. **102**(47): p. 16990-5.
41. Lindsley, C.W., et al., *Allosteric Akt (PKB) inhibitors: discovery and SAR of isozyme selective inhibitors.* Bioorg Med Chem Lett, 2005. **15**(3): p. 761-4.
42. Morris, E.J., et al., *Discovery of a novel ERK inhibitor with activity in models of acquired resistance to BRAF and MEK inhibitors.* Cancer Discov, 2013. **3**(7): p. 742-50.
43. Monasky, M.M., et al., *Dissociation of force decline from calcium decline by preload in isolated rabbit myocardium.* Pflugers Arch, 2008. **456**(2): p. 267-76.
44. Fusi, L., et al., *Minimum number of myosin motors accounting for shortening velocity under zero load in skeletal muscle.* J Physiol, 2017. **595**(4): p. 1127-1142.
45. Planelles-Herrero, V.J., et al., *Mechanistic and structural basis for activation of cardiac myosin force production by omecamtiv mecarbil.* Nat Commun, 2017. **8**(1): p. 190.
46. Snoberger, A., et al., *Human hypertrophic cardiomyopathy mutation R712L suppresses the working stroke of cardiac myosin and can be rescued by omecamtiv mecarbil.* bioRxiv, 2020: p. 2020.10.02.323782.

bioRxiv preprint doi: https://doi.org/10.1101/2020.11.10.375493; this version posted November 10, 2020. The copyright holder for this preprint (which was not certified by peer review) is the author/funder. All rights reserved. No reuse allowed without permission.

47. Toepfer, C.N., et al., *Myosin Sequestration Regulates Sarcomere Function, Cardiomyocyte Energetics, and Metabolism, Informing the Pathogenesis of Hypertrophic Cardiomyopathy.* Circulation, 2020. **141**(10): p. 828-842.
48. Olivotto, I., et al., *Mavacamten for treatment of symptomatic obstructive hypertrophic cardiomyopathy (EXPLORER-HCM): a randomised, double-blind, placebo-controlled, phase 3 trial.* Lancet, 2020. **396**(10253): p. 759-769.
49. Clippinger, S.R., et al., *Disrupted mechanobiology links the molecular and cellular phenotypes in familial dilated cardiomyopathy.* Proc Natl Acad Sci U S A, 2019. **116**(36): p. 17831-17840.
50. Pioner, J.M., et al., *Isolation and Mechanical Measurements of Myofibrils from Human Induced Pluripotent Stem Cell-Derived Cardiomyocytes.* Stem Cell Reports, 2016. **6**(6): p. 885-896.
51. Machackova, J., J. Barta, and N.S. Dhalla, *Myofibrillar remodeling in cardiac hypertrophy, heart failure and cardiomyopathies.* Can J Cardiol, 2006. **22**(11): p. 953-68.
52. van Eldik, W., et al., *Z-disc protein CHAPb induces cardiomyopathy and contractile dysfunction in the postnatal heart.* PLoS One, 2017. **12**(12): p. e0189139.
53. Luther, P.K., et al., *Heterogeneity of Z-band structure within a single muscle sarcomere: implications for sarcomere assembly.* J Mol Biol, 2003. **332**(1): p. 161-9.
54. Manalo, A., et al., *Loss of CENP-F Results in Dilated Cardiomyopathy with Severe Disruption of Cardiac Myocyte Architecture.* Sci Rep, 2018. **8**(1): p. 7546.
55. Davis, J., et al., *A Tension-Based Model Distinguishes Hypertrophic versus Dilated Cardiomyopathy.* Cell, 2016. **165**(5): p. 1147-1159.
56. Sommese, R.F., et al., *Molecular consequences of the R453C hypertrophic cardiomyopathy mutation on human beta-cardiac myosin motor function.* Proc Natl Acad Sci U S A, 2013. **110**(31): p. 12607-12.
57. Spudich, J.A. and S. Watt, *The regulation of rabbit skeletal muscle contraction. I. Biochemical studies of the interaction of the tropomyosin-troponin complex with actin and the proteolytic fragments of myosin.* J Biol Chem, 1971. **246**(15): p. 4866-71.
58. Sung, J., et al., *How to Measure Load-Dependent Kinetics of Individual Motor Molecules Without a Force-Clamp.* Methods Enzymol, 2017. **582**: p. 1-29.
59. Berg-Sørensen, K. and H. Flyvbjerg, *Power spectrum analysis for optical tweezers.* Review of Scientific Instruments, 2004. **75**(3): p. 594-612.
60. Veigel, C., et al., *The motor protein myosin-I produces its working stroke in two steps.* Nature, 1999. **398**(6727): p. 530-3.
61. Kron, S.J., et al., *An approach to reconstituting motility of single myosin molecules.* J Cell Sci Suppl, 1991. **14**: p. 129-33.
62. Dweck, D., A. Reyes-Alfonso, Jr., and J.D. Potter, *Expanding the range of free calcium regulation in biological solutions.* Anal Biochem, 2005. **347**(2): p. 303-15.
63. De La Cruz, E.M. and E.M. Ostap, *Kinetic and equilibrium analysis of the myosin ATPase.* Methods Enzymol, 2009. **455**: p. 157-92.

bioRxiv preprint doi: https://doi.org/10.1101/2020.11.10.375493; this version posted November 10, 2020. The copyright holder for this preprint (which was not certified by peer review) is the author/funder. All rights reserved. No reuse allowed without permission.

64. Dawson, J.F., et al., *Structure of an F-actin trimer disrupted by gelsolin and implications for the mechanism of severing.* J Biol Chem, 2003. **278**(2): p. 1229-38.
65. Kodo, K., et al., *iPSC-derived cardiomyocytes reveal abnormal TGF-beta signalling in left ventricular non-compaction cardiomyopathy.* Nat Cell Biol, 2016. **18**(10): p. 1031-42.
66. Wang, G., et al., *Modeling the mitochondrial cardiomyopathy of Barth syndrome with induced pluripotent stem cell and heart-on-chip technologies.* Nat Med, 2014. **20**(6): p. 616-23.
67. McQuin, C., et al., *CellProfiler 3.0: Next-generation image processing for biology.* PLoS Biol, 2018. **16**(7): p. e2005970.
68. Mann, C.K., et al., *Force-dependent recruitment from myosin OFF-state increases end-systolic pressure-volume relationship in left ventricle.* Biomech Model Mechanobiol, 2020. **19**(6): p. 2683-2692.
69. Chung, C.S., C.W. Hoopes, and K.S. Campbell, *Myocardial relaxation is accelerated by fast stretch, not reduced afterload.* J Mol Cell Cardiol, 2017. **103**: p. 65-73.
70. Linari, M., et al., *Stiffness and fraction of Myosin motors responsible for active force in permeabilized muscle fibers from rabbit psoas.* Biophys J, 2007. **92**(7): p. 2476-90.